ELSEVIER

Contents lists available at ScienceDirect

### Estuarine, Coastal and Shelf Science

journal homepage: www.elsevier.com/locate/ecss



# Spatial variation of cold front wind-driven circulation and quasi-steady state balance in Lake Pontchartrain Estuary



Wei Huang, Chunyan Li\*

Department of Oceanography and Coastal Science, College of the Coast and Environment, Louisiana State University, Baton Rouge, LA 70803, USA

#### ABSTRACT

Circulation in a low-salinity estuary with restricted openings to the ocean is mainly driven by wind and to a lesser extent by water level fluctuations at the open boundaries. Numerical model experiments are conducted using a baroclinic Finite Volume Community Ocean Model (FVCOM) for wind-driven circulations during a period encompassing a total of 16 cold fronts in the Lake Pontchartrain Estuary. The work is focused on the examination of the spatial structure of circulation in response to local and remote winds. A quasi-steady state balance between the surface slope and wind stress is further analyzed. The accuracy of the balance is evaluated by comparing the FVCOM calculated surface slope with that from the steady state balance equation. Results show that this balance is more accurate in the cross-estuary direction than that in the along-estuary direction ( $R^2 \sim 0.94$  vs. 0.60). This difference in the accuracy of the quasi-steady state balance between the cross- and along-estuary directions is caused by the open boundary - a tidally-induced mean slope exists. In addition, even if the tidal effect is removed, the accuracy still decreases toward the open end for slopes in both directions. Remote wind effect and residual flow through the eastern open boundary tend to introduce a departure from the quasi-steady state balance in both along- and cross-estuary directions. Remote wind effect decreases into the interior due to bottom friction. Local wind effect tends to produce downwind flows in coastal, shallow water regions and on the surface, but upwind flows near the bottom, a result consistent with barotropic wind-driven circulations; while the remote wind effect is important mostly near the open boundary. Furthermore, quasi-steady state balance is more accurate in the along-estuary direction before cold front passages than after, because of the relatively higher occurrence of the wind in that direction before the cold fronts than after.

#### 1. Introduction

Wind can significantly impact hydrodynamics in estuaries and coastal waters including water transports (Wong, 1987; Buijsman and Ridderinkhof, 2007; Wong et al., 2009); subtidal water level variations (Dzwonkowski et al., 2014); circulations (Sanay and Valle-Levinson, 2005; Schoen, 2014; Herrling and Winter 2015); salinity distributions (Ralston et al., 2008); mixing (Scully et al., 2005); sediment transport (Roberts et al, 1989, 2015; Kemp et al., 1980; Crout and Hamiter, 1981; Bloesch, 1995); and larval distribution (Scheffer, 2004). Winds affect estuarine circulation and water level through different mechanisms. Under barotropic conditions, the wind induced surface flow tends to be in the direction of wind, particularly in shallow waters, while on the other hand, the flow in deeper water or bottom layer tends to be against the wind (Engelund, 1973; Csanady, 1973; Falconer et al., 1991; Gibbs et al., 2016; Li et al., 2018a).

To illustrate, wind can induce two-layered circulation as shown in the East River (Filadelfo et al., 1991), which is also uncovered in Delaware Bay region and is attributed to the geomorphology effect and mass balance requirement (Garvine, 1991). Winds can produce seiches (Csanady, 1968b), alter thermocline slopes, and induce strong currents

in coastal zones by raising or depressing the thermocline (Csanady, 1968a). Both uniform wind varying with time and steady wind can produce a strong boundary current (Csanady, 1968b).

Previous studies have revealed that wind induced water volume exchanges and water level variations in the Gulf of Mexico can be comparable to, if not greater than, tidal exchanges (Feng and Li, 2010). In northern Gulf of Mexico, where tidal amplitudes are small, wind plays an important role in controlling the water exchanges. Winds associated with winter cold fronts provide major force for the water exchanges between the bay and coastal water in the Gulf of Mexico (Smith, 1977). For example, strong northerly winds during winter storms are responsible for more than 1 m of water level variations and rapid flushing from the Atchafalaya bays (Walker and Hammack, 2000). Furthermore, the post-frontal winds facilitate the offshore transport of plume water out of the Atchafalaya bay (Cobb et al., 2008). In addition, an analysis to the hydrodynamic response to 76 atmospheric fronts in a tidal channel in the southern Louisiana (Li et al., 2018b) reveals that the weather effect determines subtidal flows: cold (warm) fronts produce outward (inward) transports, similar to Weeks et al. (2018). East wind can drive saltwater intrusion through the remote wind effect (Lin et al., 2016). In short, winds, especially cold front

E-mail address: cli@lsu.edu (C. Li).

<sup>\*</sup> Corresponding author.

winds are significant in controlling hydrodynamics of coastal waters.

Wang and Elliott (1978) and Elliott (1978) investigate the local and non-local wind effects, and conclude that the alongshore non-local wind is responsible for setting up the up-bay propagation of coastal sea level fluctuations. Such non-local effect also exists at the mouth of Chesapeake Bay (Wong and Garvine, 1984). Garvine (1985) presents a barotropic analytical model showing that remote wind is responsible for the overall water level variations inside the estuary, which is confirmed by additional studies, e.g. by Wong (2002), Wong and Valle-Levinson (2002), Snedden et al. (2007), and Casares-Salazar and Mariño-Tapia (2016). Here the remote wind effect is defined as the water level variations at the mouth of an estuary due to weather forcing away from the estuary, which depends on the large-scale atmospheric conditions and the ocean dynamics. The remote wind effect is a result of complex hydrodynamic response to nonlocal weather forcing. In contrast, the local wind effect is defined as the direct impact of surface wind stress to the hydrodynamics inside the estuary. In reality, an estuary is under both remote and local wind forcing, which we call the combined effect.

Even though the water level variations are determined by remote wind, local wind is responsible for the sub-tidal current (Wong and Moses, 1998). Specifically, under local winds, flows in shallow (deep) waters are downwind (upwind) (Wong, 1994). Local wind produces surface slope variations (Guo and Valle-Levinson, 2008; Huang and Li, 2017), while remote wind generates the overall water level variations in the estuary. In addition, local wind leads to a quasi-steady state balance between the 40-hr low-pass filtered wind stress and the surface slope induced pressure gradient force (Huang and Li, 2017), which is quite accurate even when the wind changes with time (Li et al., 2018a). This balance is also satisfied in Barataria Bay of southern Louisiana (Li et al., 2019b) and Elson Lagoon in the Arctic (Li et al., 2019a). Furthermore, any changing wind can produce a seiche that dissipates within 2–3 cycles or a few hours in Lake Pontchartrain (Li et al.,

2018a). However, the effects of local and remote winds on the circulation inside an estuarine lake with limited connection to the ocean under baroclinic conditions have not been adequately examined.

In this paper, we will examine how remote and local winds impact the circulations in the low-salinity Lake Pontchartrain. Several numerical experiments are designed to accomplish these goals: 1) examine the circulations of local wind, remote wind, and both local and remote winds with baroclinicity included; 2) quantify the response of the velocity field to different wind conditions in different parts of the estuary; and 3) further examine the quasi-steady state balance in more detail under baroclinic conditions and different wind conditions associated with 16 cold front events.

#### 2. Study site: Lake Pontchartrain and previous studies

Lake Pontchartrain (Fig. 1a) is located in the southeastern Louisiana, USA, covering an area of about  $1600\,\mathrm{km}^2$  with an average depth of about 4 m. The lake is in the center of the  $12,173\,\mathrm{km}^2$  Pontchartrain drainage basin (Keddy et al., 2007) encompassing 16 parishes in southeast Louisiana (Penland et al., 2002). Lake Pontchartrain is about 40 km along the north-south direction, and about 60 km along the east-west direction, with a total water volume of  $9.77\times10^9\,\mathrm{m}^3$  (Li et al., 2008). Lake Pontchartrain was connected to the coastal ocean mainly through three narrow channels prior to the year 2012 (Fig. 1): the Industrial Canal (closed after June 2012,  $30^\circ0'18.26''N$  and  $90^\circ1'31.86''W$ ), the Chef Menteur Pass ( $30^\circ05'03.96''N$  and  $89^\circ47'28.89''W$ ), and the Rigolets ( $30^\circ10'15.67''N$  and  $89^\circ40'27.84''W$ ). The averaged depths of the Rigolets and Chef Mentuer are  $\sim12\,\mathrm{m}$ , and that of the Industrial Canal is  $\sim9\,\mathrm{m}$  (Fig. 1b).

The physical processes of water exchange of this almost-enclosed estuary with the coastal ocean determine the transport of water, salt, nutrients, pollutants, fish larvae, and sediment (Bianchi and Argyrou,

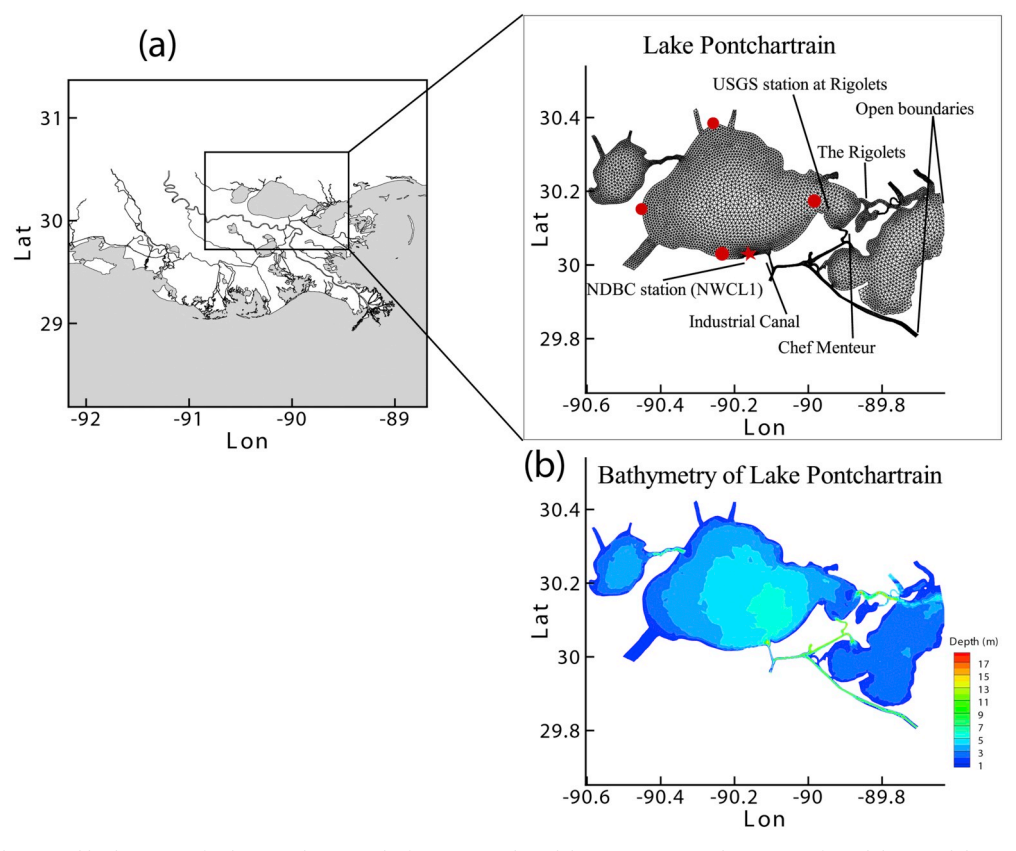


Fig. 1. Study site, mesh (a), and bathymetry of Lake Pontchartrain (b) for numerical model. Star represents the station of wind data. Red dots are the four sites used to calculate surface slopes.

1997; Georgiou et al., 2009; Li et al., 2008; McCorquodale et al., 2009; O'Connell et al., 2014; Roy et al., 2012; Signell and List, 1997; White et al., 2009). The hydrodynamic responses of Lake Pontchartrain to weather, including hurricanes and winter storms, and the subtidal water exchanges with the coastal ocean have been investigated using observations, analytical solutions, and numerical simulations. About 8–12% of the water flux was through the Industrial Canal. The remaining flux is roughly equally partitioned between the Rigolets and Chef Menteur (Li et al., 2010).

The water level fluctuations are correlated with wind (Chuang and Swenson, 1981). For instance, subtidal water volume exchanges through the tidal passes are on the same order of magnitude of the tidal oscillation of volume flux (Swenson and Chuang, 1983). Furthermore, when wind speed exceeds 3.0 m/s, wind dominates the circulation; when wind speed is less than 2.0 m/s, tidal effects dominate the circulation (Haralampides, 2000). The depth-averaged wind-driven circulation in the system (Georgiou, 2002; Georgiou et al., 2009) has higher amplitude in the region adjacent to the open boundary in the east. In addition, Chao et al. (2012) demonstrate a two-gyre circulation pattern during southeast wind and a return flow in the middle of the lake.

The subtidal water level gradient has a quasi-steady state balance with the wind, particularly during atmospheric cold fronts (Huang and Li, 2017; Li et al., 2018a; Li et al., 2019a, b). The scaling analysis of the wind-driven subtidal flow shows that subtidal pressure gradient term is two orders of magnitude larger than the local rate of change of the subtidal flow components (Li et al., 2019a), leading to a quasi-steady state balance. The mechanism of this quasi-steady state balance is also studied from another view of point by Li et al. (2018a) with numerical experiments for the adjustment processes under stepwise constant wind varying its direction at 15-day intervals. Results suggest that a change in wind produces a seiche that dissipates within 2-3 cycles that last for a few hours, which is much shorter than the diurnal tidal time scales (~24 h). These studies, however, use only barotropic models and the potential effect of stratification has not been examined yet. The present work will extend the work by including stratification and examine the effect of local vs. remote wind effects.

#### 3. Model description and validation

#### 3.1. FVCOM model description

A 3-D Finite Volume Community Ocean Model (FVCOM) is applied to simulate the hydrodynamics of Lake Pontchartrain with observed wind and with stratification. The focus is on the analysis of the response of circulation and surface slopes in the along- and cross-estuary directions to different wind conditions. Since Lake Pontchartrain is east-west (E-W) oriented, we also call the E-W direction the along-estuary direction, and the north-south (N–S) direction the cross-estuary direction.

The bathymetry (Fig. 1b) used in the numerical model combines the bathymetry from previous models (Li et al., 2008, 2018a; Huang and Li, 2017) and the water depth measured from vessel-based surveys (Li et al., 2009; 2010; Li and Zheng, 2016). Lake Pontchartrain has the average surface salinity of about 4 PSU, but the bottom salinity can reach 12 PSU at times (Li et al., 2008).

FVCOM model has been widely used for studying coastal ocean hydrodynamics (Chen et al., 2003; Huang et al., 2008; Liu et al., 2015), especially for regions with complicated topography (e.g. Huang et al.,

2011). The governing equations are (Chen et al., 2003):

$$\frac{\partial u}{\partial t} + u \frac{\partial u}{\partial x} + v \frac{\partial u}{\partial y} + w \frac{\partial u}{\partial z} - fv = -\frac{1}{\rho_0} \frac{\partial P}{\partial x} + \frac{\partial}{\partial z} \left( K_m \frac{\partial u}{\partial z} \right) + F_u$$
 (1)

$$\frac{\partial v}{\partial t} + u \frac{\partial v}{\partial x} + v \frac{\partial v}{\partial y} + w \frac{\partial v}{\partial z} + fu = -\frac{1}{\rho_0} \frac{\partial P}{\partial y} + \frac{\partial}{\partial z} \left( K_m \frac{\partial v}{\partial z} \right) + F_v$$
 (2)

$$\frac{\partial w}{\partial t} + u \frac{\partial w}{\partial x} + v \frac{\partial w}{\partial y} + w \frac{\partial w}{\partial z} = -\frac{1}{\rho_0} \frac{\partial p}{\partial z} + \frac{\partial}{\partial z} \left( K_m \frac{\partial w}{\partial z} \right) + F_w - g \tag{3}$$

$$\frac{\partial u}{\partial x} + \frac{\partial v}{\partial y} + \frac{\partial w}{\partial z} = 0 \tag{4}$$

$$\frac{\partial T}{\partial t} + u \frac{\partial T}{\partial x} + v \frac{\partial T}{\partial y} + w \frac{\partial T}{\partial z} = \frac{\partial}{\partial z} \left( K_h \frac{\partial T}{\partial z} \right) + F_T \tag{5}$$

$$\frac{\partial S}{\partial t} + u \frac{\partial S}{\partial x} + v \frac{\partial S}{\partial y} + w \frac{\partial S}{\partial z} = \frac{\partial}{\partial z} \left( K_h \frac{\partial S}{\partial z} \right) + F_S \tag{6}$$

$$\rho = \rho(T, S, p) \tag{7}$$

where x, y, z are the three axes in the east, north, and vertical directions, respectively; u, v, w are the x, y, z velocities, respectively,  $\rho_0$  is the mean density; P the total pressure of air and water; f the Coriolis parameter; g the gravitational acceleration;  $K_h$  the horizontal eddy diffusion coefficient,  $K_m$  the vertical eddy diffusion coefficient, determined by the Mellor and Yamada (1982) level-2.5 (MY-2.5) turbulent closure scheme modified by Galperin et al. (1988); T the temperature, S the salinity,  $F_w$  the diffusion term of the vertical momentum, and  $F_u$ ,  $F_v$ ,  $F_T$ , and  $F_S$  are the diffusion terms for the horizontal momentums, heat, and salt, respectively.

The surface and bottom boundary conditions are:

$$K_{m}\left(\frac{\partial u}{\partial z}, \frac{\partial v}{\partial z}\right) = \frac{1}{\rho_{0}}(\tau_{xx}, \tau_{xy}), \quad w = \frac{\partial \zeta}{\partial t} + u\frac{\partial \zeta}{\partial x} + v\frac{\partial \zeta}{\partial y}, \quad at \ z = \zeta(x, y, t)$$
(8)

$$K_{m}\left(\frac{\partial u}{\partial z}, \frac{\partial v}{\partial z}\right) = \frac{1}{\rho_{0}}(\tau_{sx}, \tau_{sy}), \ w = -u\frac{\partial H}{\partial x} - v\frac{\partial H}{\partial y}, \ at \ z = -H(x, y) \tag{9}$$

where  $(\tau_{sx}, \tau_{sy})$  and  $(\tau_{bx}, \tau_{by})$  are surface wind stress and bottom stress vectors, respectively. H is the water depth and  $\zeta$  is the surface elevation.  $(\tau_{bx}, \tau_{by})$  is the bottom stress calculated by  $C_d \sqrt{u^2 + v^2}(u, v)$  where  $C_d$  is the drag coefficient and is determined by the following equation:

$$C_d = \max\left(\frac{k^2}{\ln\left(\frac{z_{ab}}{z_0}\right)^2}, 0.0025\right)$$
(10)

where k is the von Karman constant (0.4);  $z_0$  is the bottom roughness parameter, and  $z_{ab}$  is the height above the bottom.

#### 3.2. The computational mesh and model setup

The computational mesh for the model (Fig. 1a) contains 6053 nodes and 10580 triangular cells. There are a total of 20 vertical sigma layers with a finest horizontal resolution of approximately 50 m. The time step for the external mode is 1 s. The time interval for output is 30 min. The water elevation prescribed at the open boundary is either predicted tidal elevation or observed water level (both obtained from NOAA). The wind is spatially uniform for the entire domain but varies

**Table 1**Design of numerical experiment with different open boundary condition and atmospheric forcing.

	Exp. 1	Exp. 2	Exp. 3	Exp. 4
Open boundary condition	Observed water level	Tide	Observed water level	Water level is 0 at all the time
Atmospheric forcing	Uniform wind	Uniform wind	No wind	Uniform wind

in time. The boundary temperature and salinity conditions are provided by the USGS observations. Initial temperature and salinity are set to be constants, which are 29.7  $^{\circ}\text{C}$  and 1.7 PSU, respectively. The model is run with "cold start" from Jul. 01, 2010 to Jan. 1, 2011. The first three months run is for spin up for salinity and temperature fields.

The remote and local wind effects are calculated by using different combinations of open boundary conditions and atmospheric forcing (Table 1). The combined effect is simulated by using observed water level imposed at the open boundary with a spatially uniform wind time series (Experiment 1), which is the case with measured wind driving the

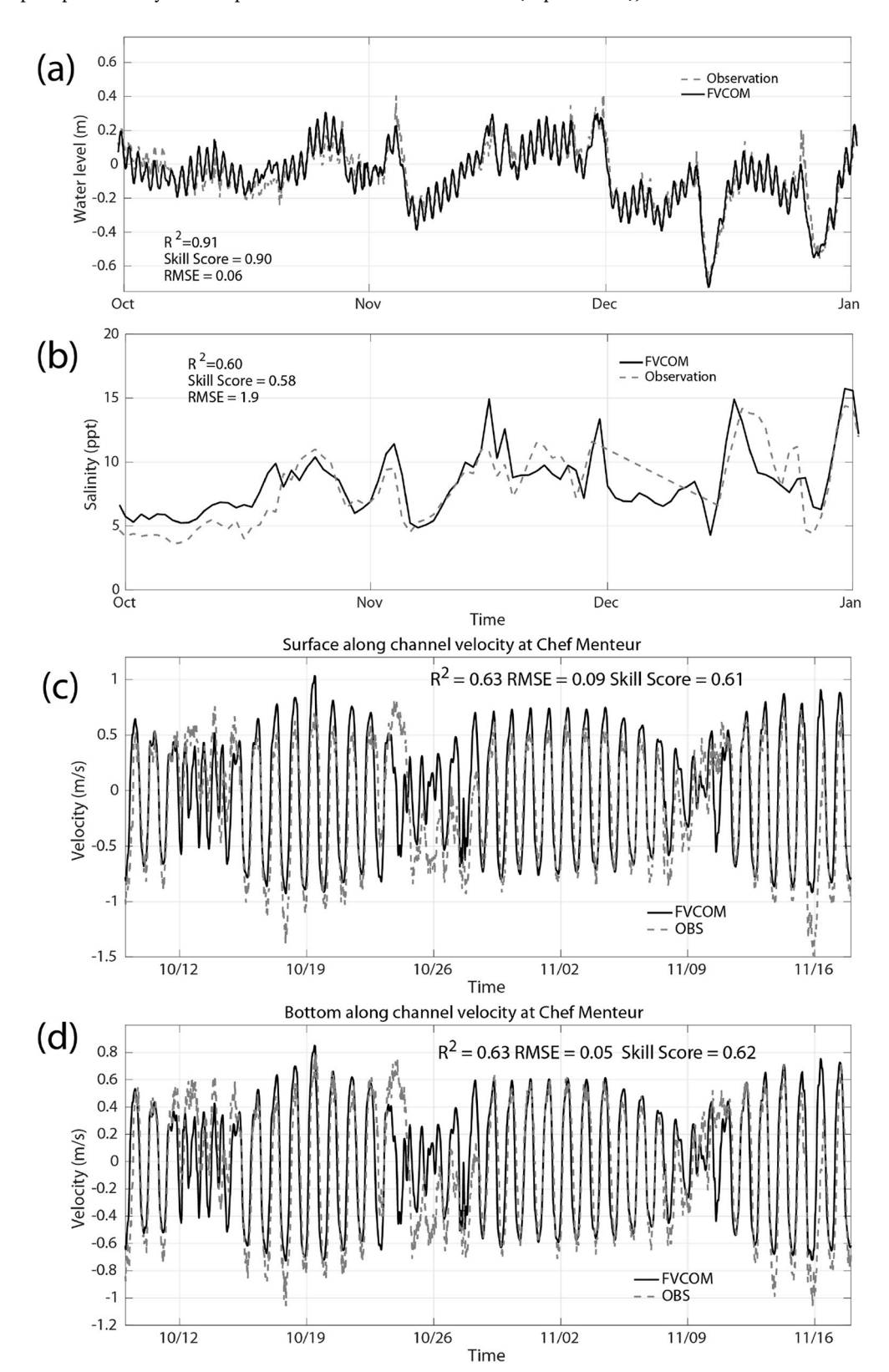


Fig. 2. Validation of (a) water level and (b) salinity for simulations from Oct. 1, 2010 to Jan. 1, 2011. Validation of (c) surface and (d) bottom along-channel velocity using observations obtained in 2008 at Chef Menteur.

model and the measured water level as the open boundary condition. The local wind effect is calculated by specifying tidal elevation at the open boundary plus a spatially uniform wind (Experiment 2). The remote wind effect is simulated by imposing the observed water elevation at the open boundary and excluding local wind forcing (Experiment 3). Since the non-tidal change of the observed water level elevation is from a remote region, the sub-tidal variation inside the basin, obtained by a low-pass filtering of the model results, is mainly driven by wind and the remote wind effect. Although the low-pass filtering removes the tidal oscillations, a tidally induced water level gradient (Li and O'Donnel, 1997) can still remain. For comparison with Experiment 3, Experiment 4 is driven only by local wind, in which the water level at the open boundary is set to be 0 while allowing free water exchange with the outside, so that the tidally induced variation is excluded.

#### 3.3. Data and forcing

Water level and weather data used here are from NOAA's National Ocean Service Station NWCL1 (8761927), which is located at 30°1′37"N, 90°6′46"W (middle south shore of Lake Pontchartrain) (red star in Fig. 1). The salinity data are from the USGS station, Rigolets at Hwy 90 near Slidell (USGS, 2010011089442600, 30°10′01" N and 89°44′26"W), from Oct. 1, 2010 to Jan. 1, 2011. Current velocity data used for the model validation were measured by an Acoustic Doppler Current Profiler (ADCP) deployed between Oct. 9 and Nov. 18, 2008 in Chef Menteur (Fig. 1). The ADCP was deployed at the bottom of the

inlets, looking upward with vertical bins of  $0.25 \,\mathrm{m}$  (Li et al., 2010). The coordinate system at the inlet is rotated so the axes are aligned in the along-channel and cross-channel directions, respectively. The cross-channel velocity is ignored here as we are only interested in the flows in and out of the estuary. Positive along channel velocity means a flow into the estuary.

The model is forced by weather, river discharge, and water level variations at the open boundary. The weather forcing includes the surface air pressure, and wind stress using the wind data scaled at 10m above the mean sea level for the period between Jul. 1, 2010 and Jan. 1, 2011. Daily river discharge data for the model input are obtained from the USGS stations of Pearl River (USGS 02490500), East Pearl River (USGS 02492110), Amite River (USGS 07380120), Tangi River (USGS 07375500), Tchefuncte River (USGS 07375000), and Tickfaw River (USGS 07376000) for Jul. 1, 2010 to Jan. 1, 2011. The daily salinity and temperature data used for forcing the open boundaries are obtained from USGS stations at Mississippi Sound (ID: 300722089150100) and Black Bay (ID: 07374526) from Jul. 1, 2010 to Jan. 1, 2011.

#### 3.4. Validation

The skill scores of the FVCOM computed water level (Fig. 2a) and salinity (Fig. 2b) from Oct. 1, 2010 to Jan. 1, 2011 are excellent (0.9), and very good (0.58), respectively, using the definition of Allen et al. (2007) and Wu et al. (2011). During this time period, there are no data for velocity. The velocity is validated for a different time period with

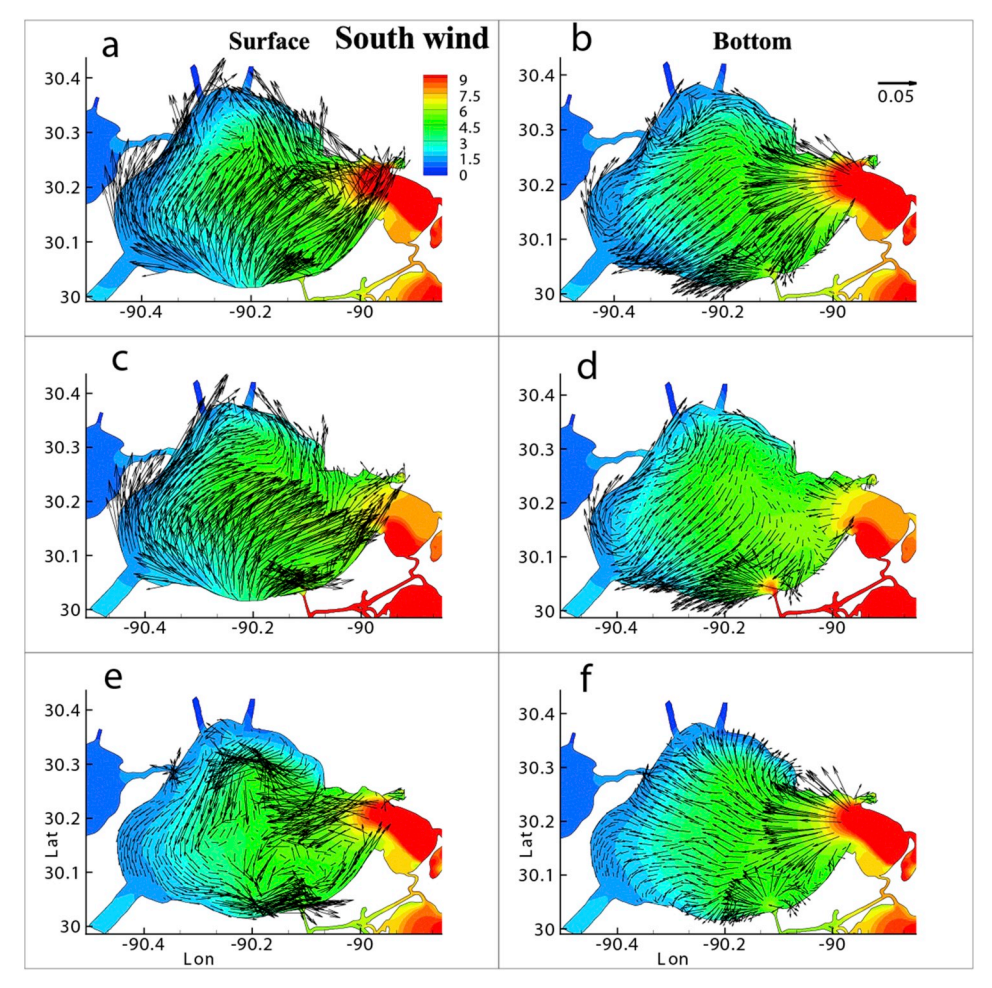


Fig. 3. Circulation under southerly wind (08:00 UTC on Dec 16, 2010). Left column shows the surface circulation (a, combined effect, c, local wind, and e, remote wind effect). Right column represents bottom circulation (b, combined effect, d, local wind, and f, remote wind effect). Color bar represents salinity (PSU). (For interpretation of the references to colour in this figure legend, the reader is referred to the Web version of this article.)

measurements of velocity profiles using an ADCP deployed at the Chef Menteur Pass from Oct. 8, to Nov. 18, 2008. The simulated surface and bottom current velocity (Fig. 2c and d) are consistent with the observed data with skill scores of 0.61 and 0.62, respectively, which can be categorized as very good (Wu et al., 2011).

#### 4. Results

#### 4.1. The overall circulation pattern of Lake Pontchartrain

We first discuss the circulation under the easterly, westerly, northerly, and southerly to illustrate the surface and bottom circulation patterns and salinity distribution induced by the combined effect (combined current, CC), remote wind effect (remote current, RC), and local wind effect (local current, LC). Winds in four directions are chosen during the period of cold front passages: northerly wind on Nov. 27, southerly wind on Dec. 26, easterly wind on Nov. 29, and westerly wind on Nov. 16.

Under southerly (northerly) wind, the surface CC (Fig. 3a and Fig. 4a) tends to be downwind toward the northern (southern) shore in most of the interior. Near the open boundary in the east, when the water level increases at the open boundary, the CC is into the estuary through the Rigolets and Chef Menteur; when the water level is dropping, the CC is out of the estuary. The bottom CC (Figs. 3b and 4b) is upwind in the western interior, but downwind along the western shore where water is shallower. The bottom CC along the western coast turns

along the northern (southern) shore to the east after reaching the northern (southern) shore under the southerly (northerly) wind, and then joins the return flow in the deeper water area in the center, forming a clockwise (counter-clockwise) circulation in the western region of the estuary. In the eastern region, because of the water level variations at the open boundary, flows alternate in and out of the estuary and are intensified by the narrow channel of the Rigolets and Chef Menteur, thus the CC in the eastern region is essentially in the west-east directions.

Under easterly (westerly) wind, the surface CC (Fig. 5a and Fig. 6a) over most of the estuary is downwind. For the central lake, surface CC is weaker than that in the coastal area. The bottom CC (Figs. 5b and 6b) in the shallower shore region is downwind. A return flow is established from west (east) to east (west) in the interior in the western region. When this return flow meets with the inflow from the two inlets in the east, it bifurcates into two branches to the south and north, respectively.

Salinity is higher (> 9 PSU) in the eastern region. Saltwater is transported into the lake through the Rigolets. In the central part of the estuary, salinity is around 4 PSU, in the coastal zone along the shore, the salinity is lower than 2 PSU. When water is flowing into the estuary (Fig. 3a and b and Fig. 5a and b), salinity in the western central region is relatively high. When water is flowing out of the estuary (Fig. 4a and b, and Fig. 6a and b), salinity in the western central region is relatively low.

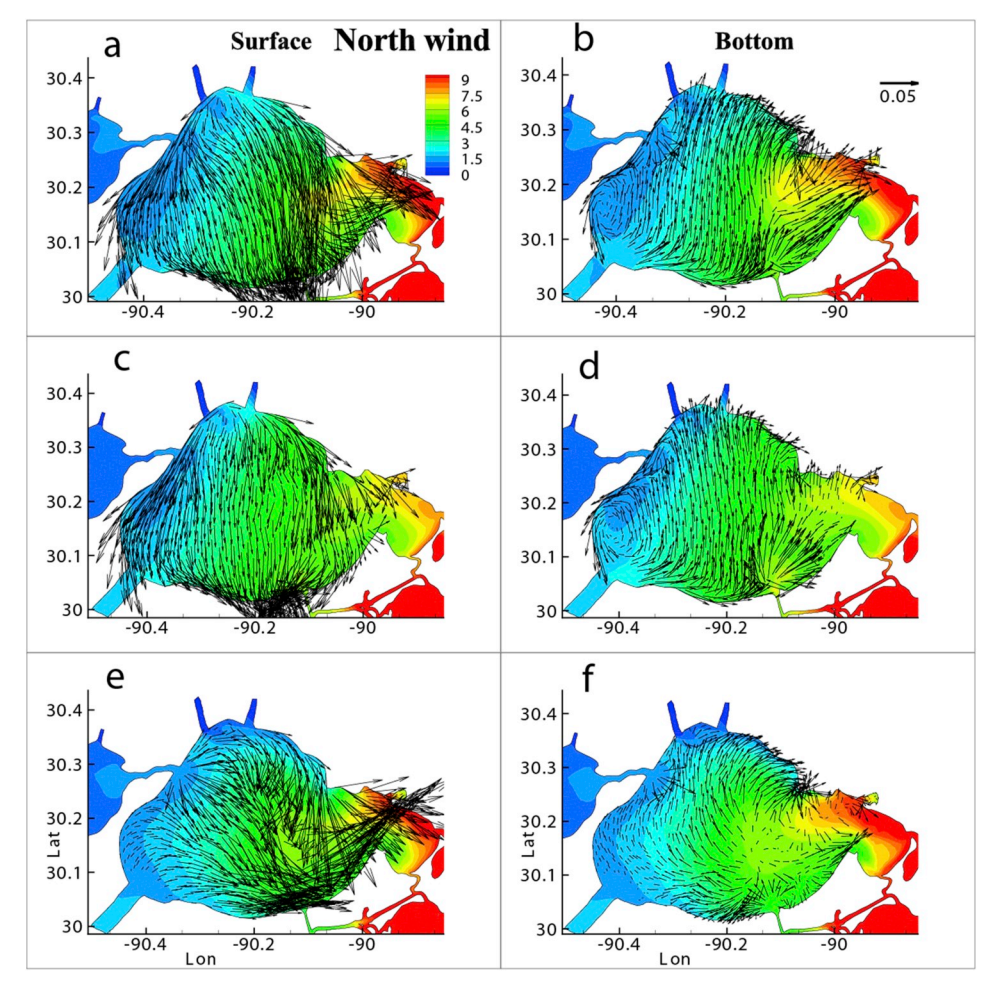


Fig. 4. Circulation under northerly wind (00:00 UTC on Nov 27, 2010). Left column shows the surface circulation (a, combined effect, c, local wind, and e, remote wind effect). Right column represents bottom circulation (b, combined effect, d, local wind, and f, remote wind effect). Color bar represents salinity (PSU). (For interpretation of the references to colour in this figure legend, the reader is referred to the Web version of this article.)

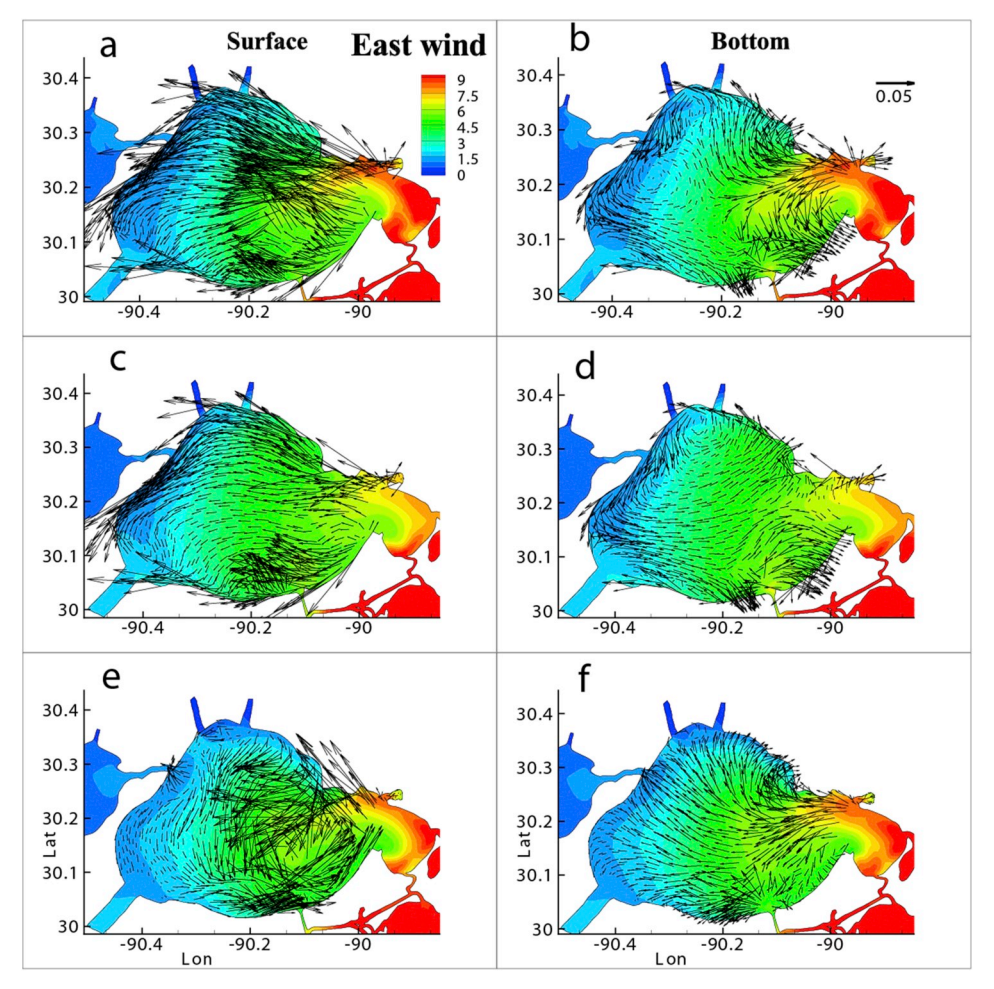


Fig. 5. Circulation under easterly wind (00:00 UTC on Nov 29, 2010). Left column shows the surface circulation (a, combined effect, c, local wind, and e, remote wind effect). Right column represents bottom circulation (b, combined effect, d, local wind, and f, remote wind effect). Color bar represents salinity (PSU). (For interpretation of the references to colour in this figure legend, the reader is referred to the Web version of this article.)

#### 4.2. Circulation pattern under local and remote wind effect

#### 4.2.1. Local wind induced circulation

Under southerly (northerly) wind, the surface LC (Figs. 3c and 4c) for the entire estuary tends to be downwind in general. The inward or outward flows through the Rigolets are not as strong as those under the combined effect, indicating that the local wind doesn't contribute significantly to the inward/outward flows through the restricted open boundary. There is a broad return flow in the bottom layer (Figs. 3d and 4d) in the central estuary, with almost the same magnitude as the total return flow (Figs. 3b and 4b). The return flow bifurcates into two branches of coastal currents in opposite directions after arriving at the northern (southern) coast, forming a clockwise (counter-clockwise) circulation in the western estuary.

When the easterly (westerly) wind dominates, the surface LC (Figs. 5c and 6c) for the coastal region has almost the same pattern inside the estuary with a magnitude comparable to that of the combined effect (Figs. 5a and 6a), flowing in the downwind direction. There is no obvious inflow or outflow from the two inlets. For the eastern region close to the restricted open boundary, the surface LC is downwind but has a different pattern compared to the CC flows. The bottom upwind return flow is more evident (Figs. 5d and 6d), resulting in a counterclockwise (clockwise) circulation.

Salinity distribution inside the lake is similar to that of the combined effect. The obvious difference is that high salinity under local wind is mainly located at the Chef Mentuer (Fig. 3c and d). During southerly wind, salinity is higher at the Industrial Canal (Fig. 3c and d).

In other cases, local winds are only responsible to distribute the salinity through Chef Menteur.

#### 4.2.2. Remote wind induced circulation

For the remote wind effect, when water is flooding into the estuary (Figs. 3e and 5e), the surface RC in the eastern side is consistent with the inflow from the open boundary. Since most of the water volume is transported through the eastern inlets (Li et al., 2008), surface RC is strong along the northeastern shore. The surface RC turns to southern shore on the western side. After the surface RC flows back to the eastern side along the southern shore, forming a counter-clockwise circulation on the surface. The bottom RC (Figs. 3f and 5f) is in the direction of the inflow from the open boundary, and bifurcates to the south and north while flowing toward the western shore.

When water is ebbing out of the estuary (Figs. 4e and 6e), the surface RC is in the direction of the outflow in most of the estuary. RC at the northeastern side is toward the south. For the bottom RC (Figs. 4f and 6f), there is a return flow in the central region. The return flow diverges into two branches as it moves toward the west.

Salinity distribution under remote wind effect is similar to that under combined effect. High salinity water is at the eastern side and is transported into the estuary through the Rigolets channel. Salinity in the Chef Menteur pass is lower than that of local wind effect. The salinity distribution in the central estuary is determined by the water exchange with the open ocean, because when the water level increases, salinity inside the estuary is higher, when water level decreases, salinity is lower.

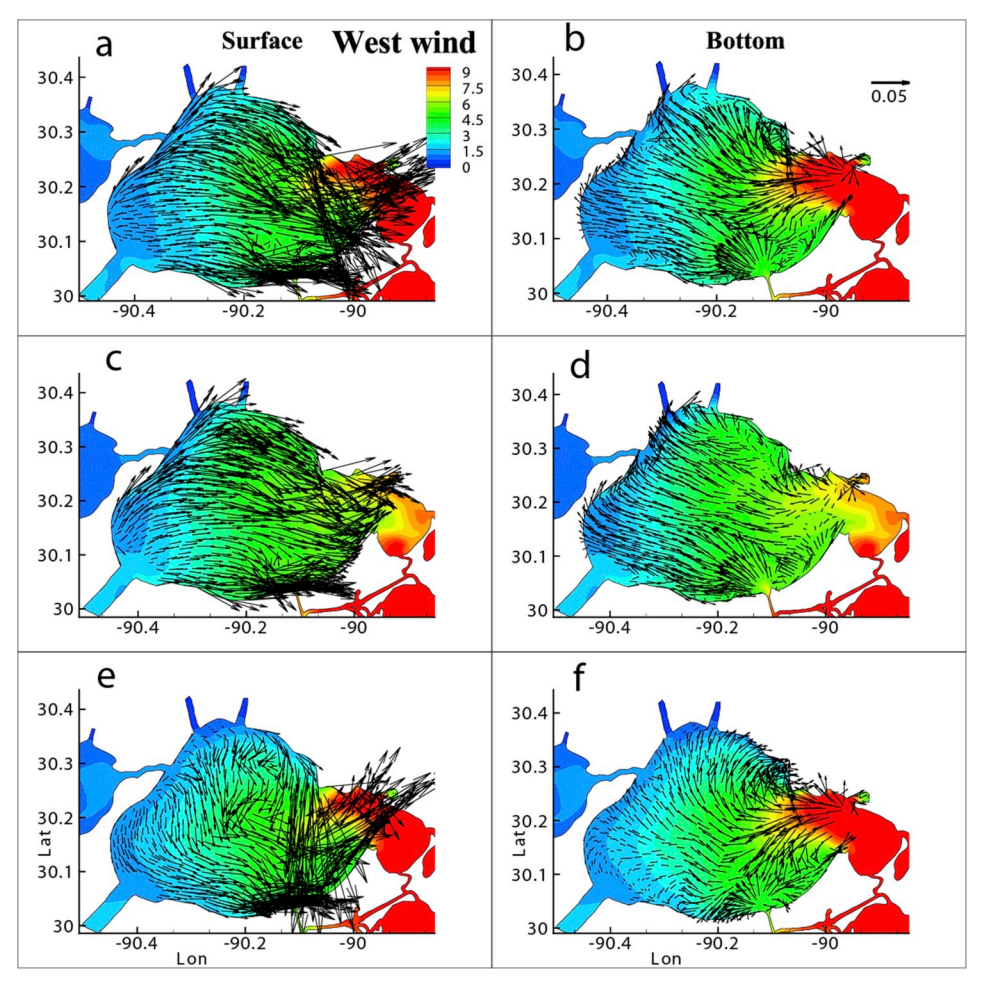


**Fig. 6.** Circulation under westerly wind (10:00 UTC on Nov 16, 2010). Left column shows the surface circulation induced by (a, combined effect, c, local wind, and e, remote wind effect). Right column represents bottom circulation (b, combined effect, d, local wind, and f, remote wind effect). Color bar represents salinity (PSU). (For interpretation of the references to colour in this figure legend, the reader is referred to the Web version of this article.)

## 4.3. Spatial distribution of velocity magnitude under local/remote wind effect

Distribution of velocity magnitude (Figs. 7–9) under different wind conditions is examined as follows. Under southerly wind (Fig. 7a,c,e), the local wind mainly influences the flows along the coast and in the western central interior, while the remote wind mainly affects the flows in the eastern and northeastern areas. The current velocity near the bottom exhibits the same features as that of the surface layer (Fig. 7b,d,f). The remote wind has the most influence in the eastern and northeastern regions and near the open boundary, while on the other hand the local wind determines flows in the coastal regions and the shallow western interior. Remote wind effect is dissipated by the bottom friction away from the eastern open boundary (Appendix).

Under easterly and westerly winds, the remote wind effects dominate the flows near the open boundary region; however, in parts of the interior, especially in the southwestern region, the remote wind effect (Fig. 8e) has almost completely disappeared due to friction; but in the central and northeastern regions, remote winds still exhibit considerable influences. For the coastal region, local wind effect is again the main contributor to circulations. These features also appear in the bottom flows (Fig. 8b,d,f).

To further examine and quantify the spatial distribution of remote and local wind effects, we have calculated the difference of the velocity magnitude between the combined effect and remote wind effect and that between the combined effect and local wind effect. The smaller the difference is, the closer the remote (local) wind effect is to the

combined effect, therefore, more important than the local (remote) wind effect. The larger difference between the combined effect and remote wind effect (Fig. 9 c, d) is mainly located in the region along the shore zones; and the larger difference between the combined effect and local wind effect reaches the maximum in the eastern region close to the open boundary (Fig. 9a), which is consistent with the previous finding that the remote wind effect is dominant in the eastern region close to the open boundary, whereas local wind effect controls the velocity along coastal regions and part of the central region. There is a region around 30.2°N and 92.1°W where both local and remote wind effects are evident.

The bottom layer circulations are shown in Fig. 9b and d. Indeed, the difference between the LC and CC in the bottom layer reaches the maximum near the open boundary (Fig. 9b) i.e. the remote wind is dominant there. In the western and southwestern shore areas, differences are larger (Fig. 9d), indicating that the local wind effect dominates.

To further quantify the relative importance of the local and remote wind effects, we calculate the ratio of total flows normalized by the combined effect with the following equations:

$$E_{LC} = \frac{sum(U_{LC})}{sum(U_{CC})} \tag{11}$$

$$E_{RC} = \frac{sum(U_{RC})}{sum(U_{CC})} \tag{12}$$

in which  $E_{LC}$  and  $E_{RC}$  represent the ratios between the local and remote

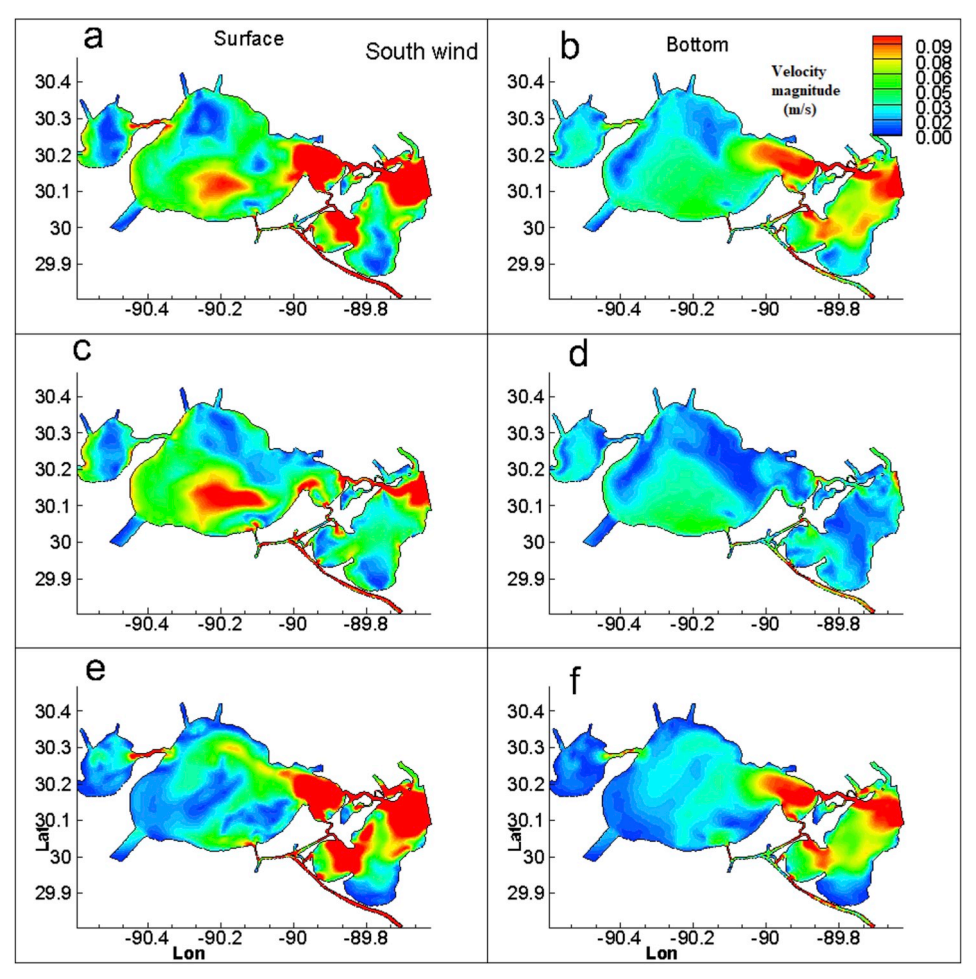


Fig. 7. Magnitude of current velocity under southerly wind. Figs. (a), (c), (e) are the velocity magnitudes in surface layer of combined effect, local wind effect, and remote wind effect, respectively, Figs. (b), (d), (f) are the velocity magnitudes in bottom layer of combined effect, local wind effect, and remote wind effect, respectively.

wind effects and the combined effect in each of the three regions (the eastern, coastal, and central regions),  $sum(U_{LC})$ ,  $sum(U_{RC})$ , and  $sum(U_{CC})$  are the summations of the velocity magnitude of each region under local wind only, remote wind only, and both local and remote winds, respectively. E<sub>LC</sub> and E<sub>RC</sub> represent the relative importance of local and remote wind effects compared with the combined effect. Note that we are not comparing with the velocity vectors at each point, and (E<sub>LC</sub> + E<sub>RC</sub>) does not necessarily equal to 1 because the combined effect is not a simple superposition of remote and local wind effects and the problem is not linear. The results show that in the coastal region, the ratio (Table 2) between local wind effect and the combined effect (ELC) is about 0.87, larger than  $E_{RC}$  (0.79), which means that the local wind effect contributes more in the regions with shallower water along the coastal zones. For the central region,  $E_{LC}$  is 0.6, smaller than  $E_{RC}$  which is 0.88, indicates the more important role the remote wind effect plays in this region. For the eastern region near the open boundary, the remote wind effect is dominant with a ratio of 1.01, compared with that for the local wind effect of 0.5.

#### 5. Discussion

#### 5.1. Quasi-steady state balance in cross- and along-estuary directions

The above discussion clearly reveals that local wind effect controls the circulations for part of the interior, particularly in shallow waters, on the surface, and most of the coastal regions. Furthermore, local wind is also the main driver of the surface slope in the along- and cross-estuary directions, and can be well approximated by a quasi-steady state force balance, which is an extension of results of Huang and Li (2017), Li et al. (2019a, b), and Li et al. (2018a) in which no stratification was considered in the models. This quasi-steady state balance is:

$$0 = -g\frac{\partial \zeta}{\partial x} + \frac{\tau_{ax}}{\rho h} \tag{13}$$

where  $\partial \zeta$  is the subtidal surface level difference in two directions,  $\partial x$  is the cross- and along-estuary distance (37 or 52 km, respectively). Four points from N, S, W, and E sites around the lake are selected. In equation (13),  $\rho$  is the water density (1024 kg/m³), h is the average water depth of 4.0 m  $\tau_{\alpha x}$  is the wind stress in the cross or along-estuary direction (Garvine, 1985):

$$\tau_{ax} = \rho_a C_d |W| W_x \tag{14}$$

where  $\rho_a$  is the air density (1.29 kg/m³),  $C_d$  is the drag coefficient of  $1.24 \times 10^{-3}$ ,  $W_x$  is the wind velocity component in the cross- or alongestuary direction with a total wind speed of W obtained from the NOAA's NDBC station NWCL1 (Fig. 1).

The study of Li et al. (2018a) indicates that the quasi-steady state is a result of a quick adjustment process under variable winds. This adjustment is a damped seiche oscillation. The periods of the oscillations are accurately verified by a numerical experiment in Lake Pontchartrain

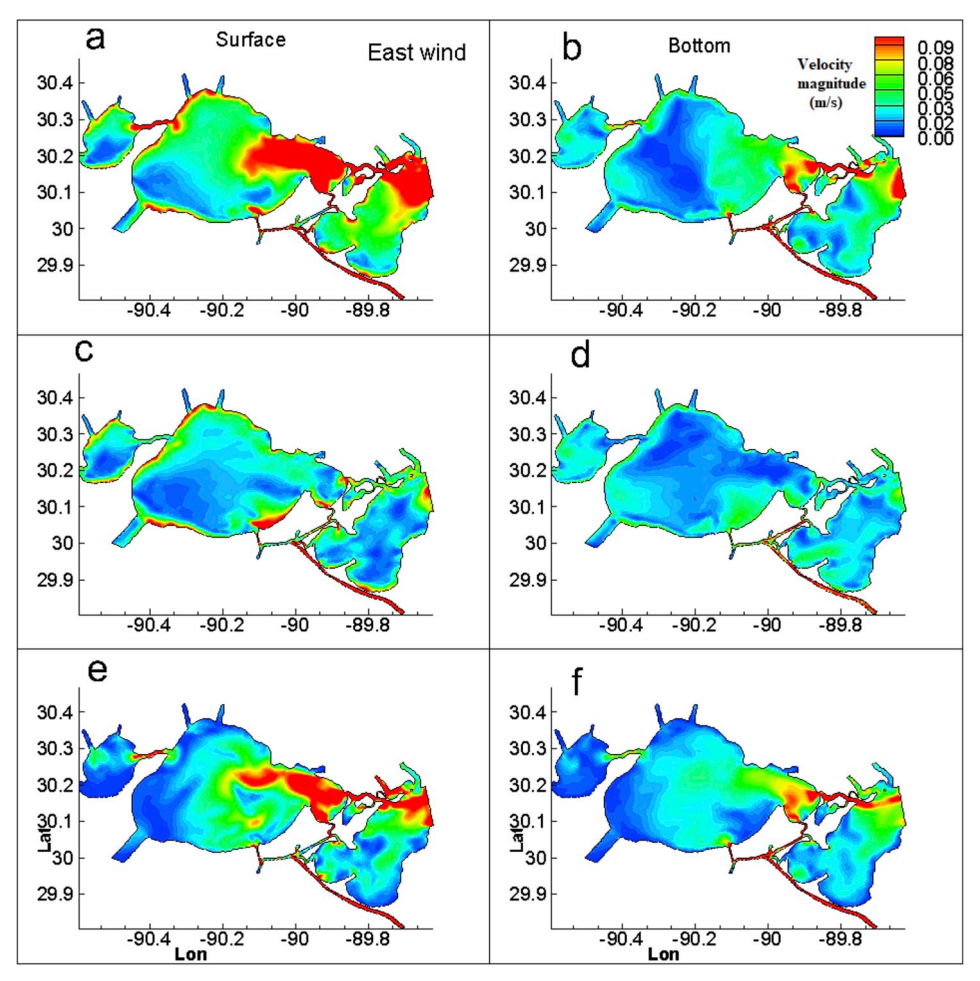


Fig. 8. Magnitude of current velocity under easterly wind. Figs. (a), (c), (e) are the velocity magnitudes in surface layer of combined effect, local wind effect, and remote wind effect, respectively, Figs. (b), (d), (f) are the velocity magnitudes in bottom layer of combined effect, local wind effect, and remote wind effect, respectively.

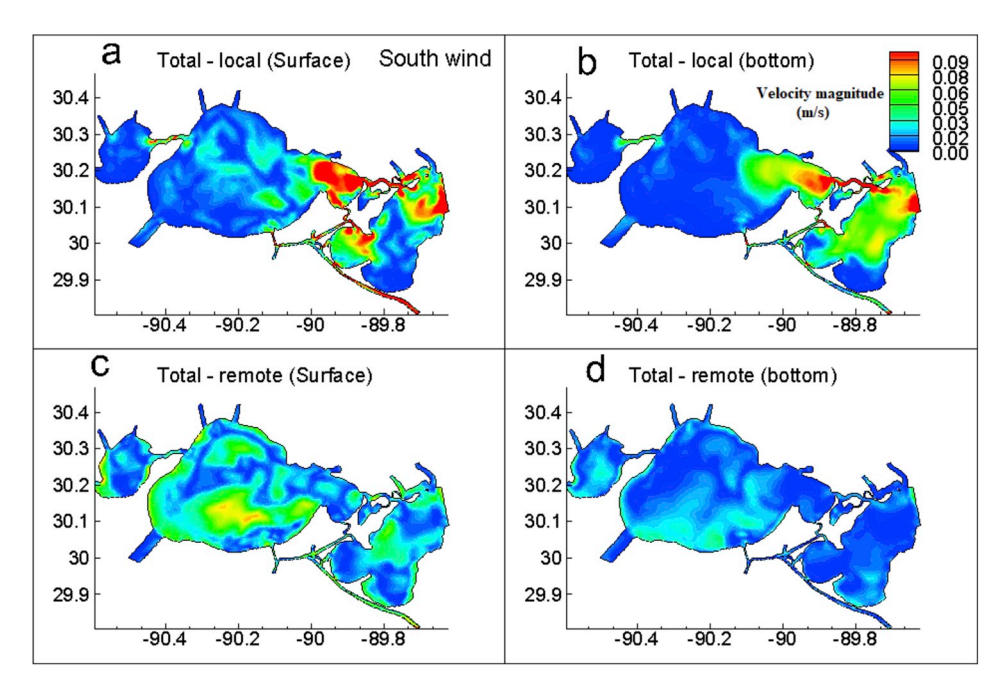


Fig. 9. Difference of magnitude between combined effect and local/remote wind effect under southerly wind. Figs. (a) and (b) are the difference of velocity magnitudes between the velocity magnitude of the combined effect and that of local wind effect in surface and bottom layers. Figs. (c) and (d) are the difference of velocity magnitudes between the velocity magnitude of combined effect and that of remote wind effect in surface and bottom layers.

 Table 2

 Ratio of local/remote wind effect comparing with the combined effect in terms of integrated velocity magnitude in three different regions.

	Open boundary region	Coastal region	Central lake region	
Local effect/combined effect	0.50	0.87	0.60	
Remote effect/combined effect	1.01	0.79	0.88	

based on the seiche oscillation period determined by

$$T = \frac{2L}{\sqrt{gh}}$$

in which T, L, g, and h are the period of seiche oscillation, the distance between two points on opposite coasts, gravitational acceleration, and mean water depth along the line, respectively (Proudman, 1953; deBoer and Maas, 2011).

The R<sup>2</sup> values in the cross- and along-estuary directions in Huang and Li (2017) are 0.83 and 0.43, respectively, indicating a difference or asymmetry in quasi-steady state balance in the cross- and along-estuary directions. Here we examine the quasi-steady state balance between wind-induced pressure gradient and wind-stress when stratification is present. The results (Fig. 10a, c) show that the cross-estuary surface slopes between Oct. 1, 2010 and Jan. 1, 2011 estimated by the quasi-steady state equation (gray dashed line) from both Experiment 2 and

Experiment 4 are in an almost perfect agreement with that calculated from the model results (black solid line). However, in the along-estuary direction, surface slope resulted from Experiment 2 (black solid line in Fig. 10b) is lower than that produced by the quasi-steady state balance (gray dashed line in Fig. 10b), leading to a lower R<sup>2</sup> (0.65) under this experimental condition. To further examine the relationships, we subtract the mean surface slopes and calculate the R<sup>2</sup> value again. The R<sup>2</sup> value (Table 3) for Experiment 1 (combined effect) in the along-estuary and cross-estuary directions are the lowest (0.60 and 0.94). After subtracting the mean slope from the simulated surface slopes, the R<sup>2</sup> value in the along-estuary direction is significantly increased to 0.96. R<sup>2</sup> values for Experiment 2 (0.95 and 0.65) are slightly higher than that for Experiment 1 (0.94 and 0.60). The demeaned R<sup>2</sup> values for Experiment 2 are increased to 0.98 in the along-estuary direction. R2 values for Experiment 4 in both directions are high and comparable (> 0.95). These results show that either subtracting the mean slope or remove the

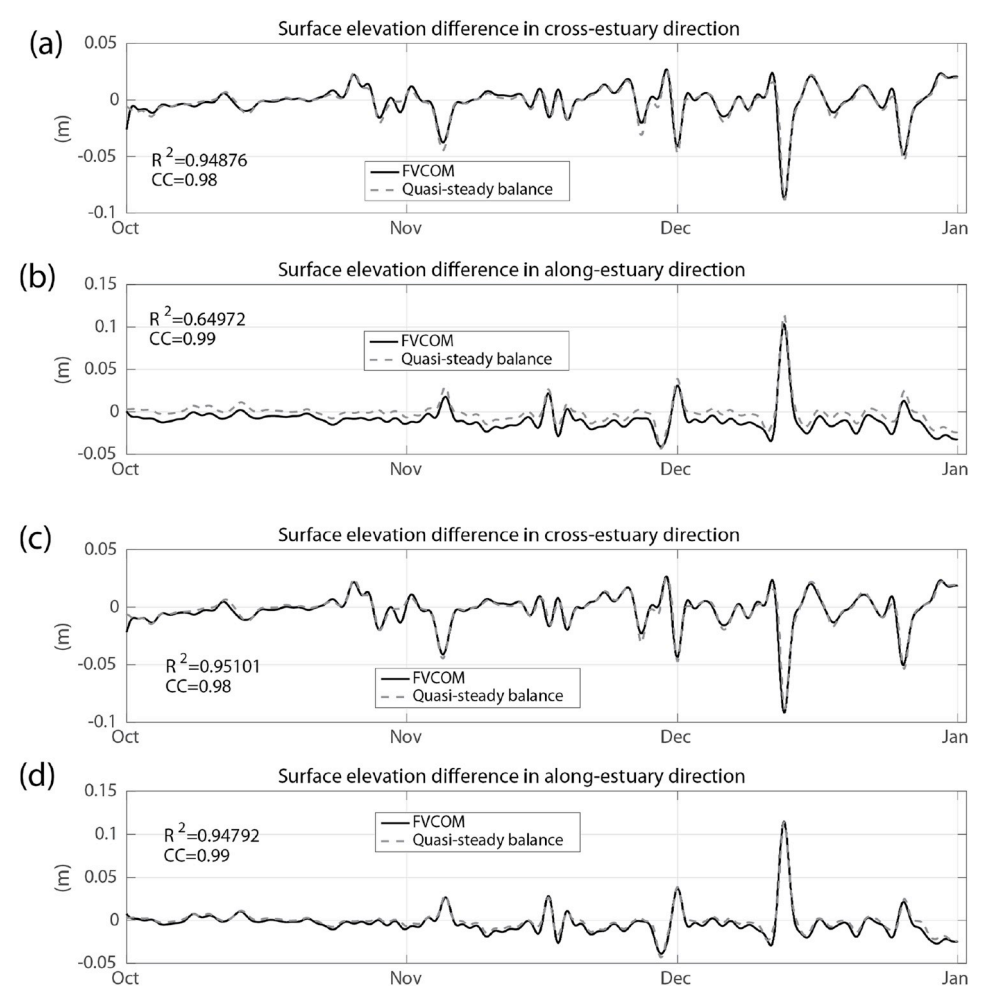


Fig. 10. Comparison between quasi-steady state balance induced surface slopes (dashed grey lines) and that calculated by the FVCOM model (solid black lines) in cross estuary (N–S) and along estuary directions (E–W). Figures a) and b) are under local wind conditions with tide at the open boundary (Experiment 2), c) and d) are under local wind conditions but without tidal forcing at the open boundary (Experiment 4).

Table 3 R square value ( $R^2$ ) and root mean squared error (RMSE) for the approximation of surface slope in cross- and along-estuary directions under combined effect, local wind effect, pure local wind effect, and remote wind effect.

	Combined effe	Combined effect (Experiment 1)		Local wind effect 1 (Experiment 2)		Local wind effect 2 (Experiment 4)	
	$R^2$	RMSE	$R^2$	RMSE	$R^2$	RMSE	
	0.94	0.0036	0.95	0.0032	0.95	0.0032	
Cross-estuary (demeaned)	0.95	0.0036	0.95	0.0031	0.95	0.0032	
Along-estuary	0.60	0.0089	0.65	0.0087	0.95	0.0035	
Along-estuary (demeaned)	0.96	0.0029	0.98	0.0023	0.97	0.0025	

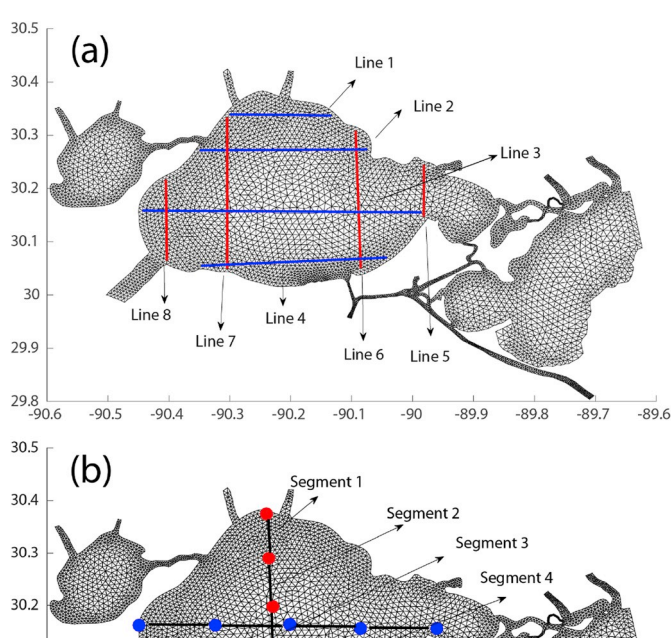
tidal input at the open boundary can increase the  ${\rm R}^2$  between the quasisteady state balance and the FVCOM results in the along-estuary direction.

The reason of the difference of R2 values in the two directions is because of the open boundary being in the east. Tide is input from the east. The shallow water of the estuary leads to a relatively high nonlinearity due to tidal oscillation (~4 m mean depth), which is the strongest at the eastern open end. The bottom friction and nonlinear tide will produce a mean slope into the lake toward the west (the subtidal or mean water level on the west being slightly higher than the east) as shown in Li and O'Donnell (1997), adding a net negative slope due to tide (see the lower curve from FVCOM results and the higher curve from the quasi-steady state balance in Fig. 10b). When the open end is closed, the tidal effect disappears and the two R<sup>2</sup> values become very close (Fig. 10c and d). Note also that even though the two directions have very different R<sup>2</sup> values, the trends are very much the same. As a result, the correlation coefficients are all high ( $CC \sim 0.98-0.99$ , Fig. 10). Since the tidally induced mean slope does not change with wind and it has much smaller variations. Consequently, the correlation coefficients between the FVCOM model results and the quasi-steady state balance equation are all high in the two directions (Fig. 10). If we subtract the mean slope or exclude tidal input at the open boundary, the  $R^2$  value in the east-west direction will increase to ~95% (Table 3), the same value to that in the north-south direction. In other words, if the tidal effect is taken away by removing the mean, the two directions appear to be the same. Alternatively, defining zero amplitude for tide at the open end will also increase the R<sup>2</sup> to about 95%.

To reinforce this argument, we have analyzed 4 more transect lines in the E-W and N–S directions, respectively, to examine the open boundary effects on the quasi-steady state.

First, 4 transects (Fig. 11a) are selected to calculate the total water level difference in both E-W and N–S directions. The N–S water level differences for lines 1–4 and the E-W water level differences for lines 5–8 are calculated using the quasi-steady state equation and FVCOM results, respectively (Fig. 12). The data are low-pass filtered and demeaned. Results show that the R<sup>2</sup> values of the E-W water level differences from north to south (Fig. 12a–d) are all higher than 0.9, however, R<sup>2</sup> values of the N–S water level differences from east to north (Fig. 12e–h) are increasing with the lowest R<sup>2</sup> being only 0.66 for the eastern-most transect, confirming again that the existence of the eastern open boundary can significantly affect the quasi-steady state balance in the eastern region.

Secondly, we select two transects (Fig. 11b) to investigate the N–S and E-W water level differences along each transect so that we can check how water level difference changes along the transects. As shown in Fig. 13, two transects are selected with 5 nodes on each transect. Calculations of water level differences from the quasi-steady state and FVCOM are done between adjacent nodes or for each segment (Fig. 13).



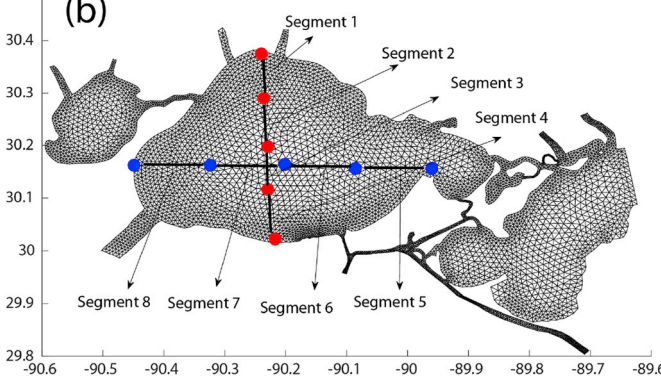


**Fig. 11.** a, Lines selected to calculate the water level difference. Lines 1–4 are in the N–S direction, lines 5–8 are in the E-W direction. b, Segments along the N–S and E-W transects. Segments 1–4 are between adjacent nodes (red dots) along the transect in the N–S direction, segments 5–8 are between adjacent nodes (blue dots) along the transect in the E-W direction. (For interpretation of the references to colour in this figure legend, the reader is referred to the Web version of this article.)

The  $R^2$  values are increasing from east to west with a value of 0.44 at the eastern-most segment and 0.94 at the western-most segment (Fig. 13a–d), i.e. the accuracy of quasi-steady state balance decreases towards the eastern open boundary, which confirms our previous conclusion that eastern open boundary effect tends to impact the quasi-steady state balance. For the transect in N–S direction (Fig. 13e–h), the  $R^2$  values are higher (exceeding 0.9) for the segments near coastal region and lower (0.85 and 0.88) for segments 2 and 3 in the central region.

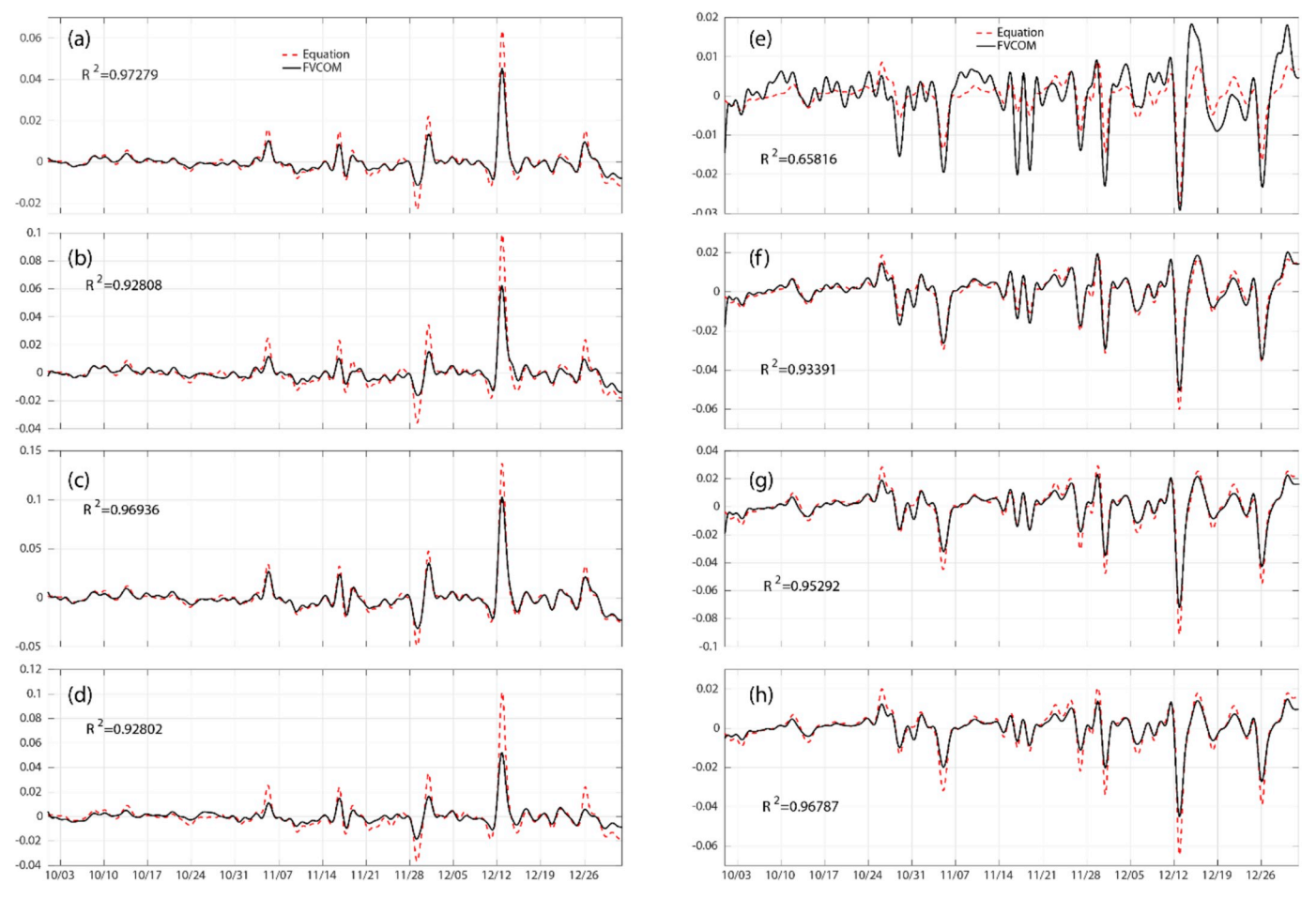


Fig. 12. Water level differences calculated from the quasi-steady state equation (dashed red lines) and that from FVCOM (solid black lines) for each line in Fig. 11a. ad are the E-W water level differences for lines 1–4 from north to south, and e-h are the N–S water level differences for lines 5–8 from east to west. (For interpretation of the references to colour in this figure legend, the reader is referred to the Web version of this article.)

#### 5.2. Quasi-steady state balance during cold fronts

Given that local wind is the main force setting up the surface slope and the change in wind regimes occurs during atmospheric cold front events (Moeller et al., 1993; Cobb et al., 2008; Feng and Li, 2010; Li and Chen, 2014), we now examine the circulations in Lake Pontchartrain from Oct. 1, 2010 to Jan. 1, 2011 during which there are 16 cold frontal passages (Table 4) and our FVCOM model run includes this time period with Experiment 2. For convenience, we define the start time of each front as the time when the cold front enters the northwestern Louisiana, and the ending time is when the cold front leaves the area at the southeastern of LA (Table 4). Changes of wind regimes associated with cold front passages can be viewed as three stages: prefrontal, frontal, and postfrontal stages. The frontal passage time is usually very short (~a few hours). Fig. 14 provides the statistics of the wind before and after the 16 cold front passages with the frequency of occurrence. Before the cold front passages (Fig. 14a), southerly wind is most frequent (more than 40%), there is also more than 20% of east/west wind, while nearly 60% of the wind after the cold front passages is northerly or northeasterly (Fig. 14b).

The quasi-steady state equation is applied to calculate the approximated surface slopes, before and after each of the cold front passages. Comparing with the FVCOM calculated surface slopes from Experiment 2 (local wind with tidal forcing at open boundary), the R<sup>2</sup>

values are computed. Table 5 shows that before the cold front, the average  $R^2$  values in the cross- and along-estuary directions are 0.55 and 0.67, respectively. The higher average  $R^2$  in the along-estuary direction is apparently caused by the more frequent easterly or westerly winds before the cold fronts. However, the post-front average  $R^2$  values in the cross- and along-estuary directions are 0.66 and 0.57, respectively. The higher average  $R^2$  in the cross-estuary direction is due to the strong northerly wind after the cold front passages.

#### 6. Summary

In this study, the spatial structures of velocity field in the Lake Pontchartrain Estuary are studied for local, remote, and combined wind effects. A baroclinic FVCOM has been applied in the study with four sets of numerical experiments for the hydrodynamics of wind-driven circulations under winds from a sequence of 16 cold fronts. The general circulation pattern of remote and local wind effects can be described below. The remote wind effect facilitates the inflow and outflow through the inlets in the eastern side, and has a great influence in the eastern interior or the region close to the open boundary. Currents under local wind tend to be in the downwind direction in shallow coastal region, with a return flow against the wind at near bottom, similar to the barotropic circulation (Li et al., 2018a; Li et al., 2019b). Besides, salt transported through the Rigolets is mainly controlled by

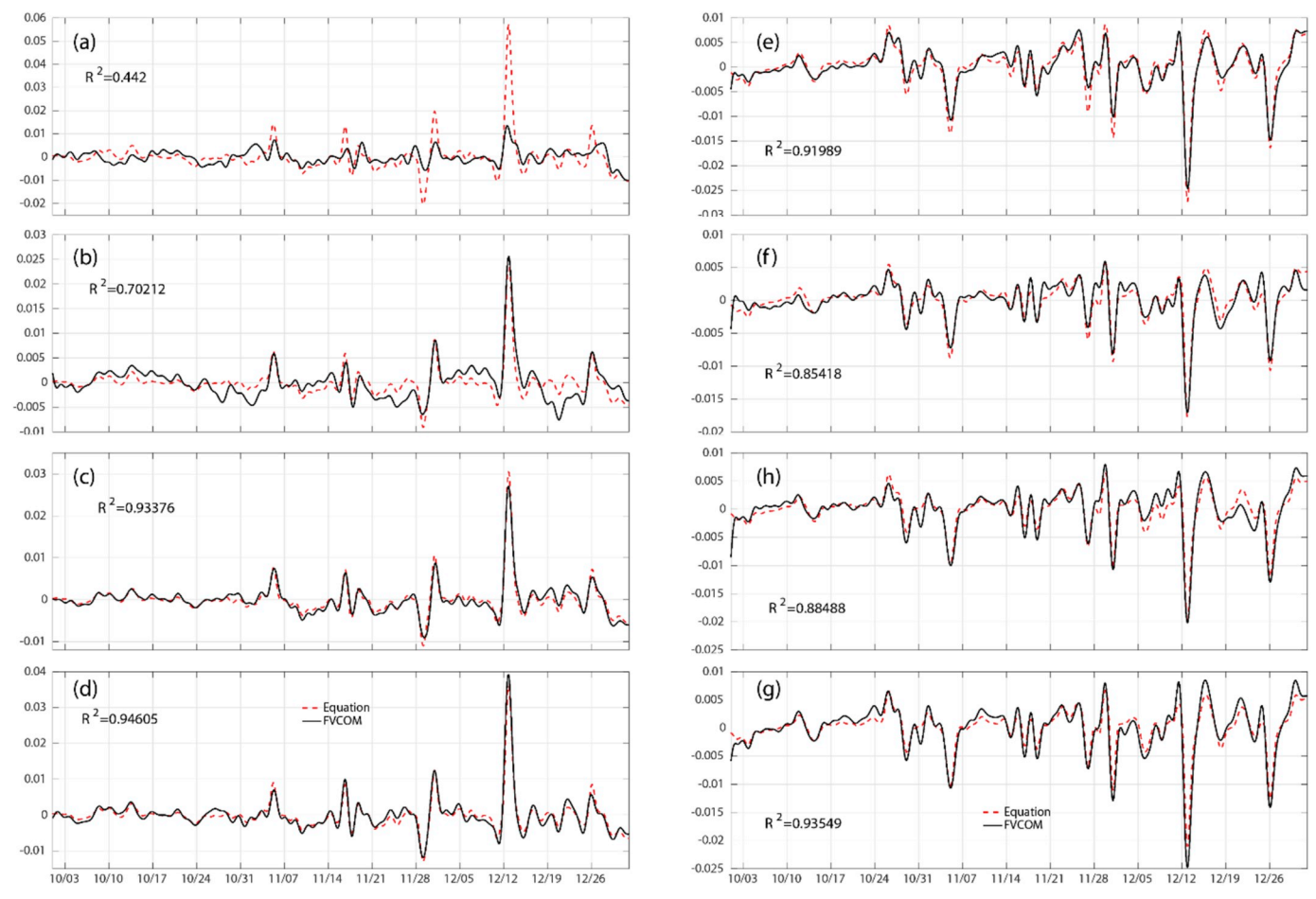


Fig. 13. Water level differences calculated from the quasi-steady state equation (dashed red lines) and that from FVCOM results (solid black lines) for each segment in Fig. 11b. a-d are the water level differences for segments 5–8 along transect in the E-W direction, e-h are for the segments 1–4 along transect in the N–S direction. (For interpretation of the references to colour in this figure legend, the reader is referred to the Web version of this article.)

Table 4
Entering and leaving date and time of the 16 cold front events affecting Louisiana (LA) State from Oct. 01 to Dec. 31, 2010.

	Date and time entering LA				Date and time	Date and time leaving LA			
1	2010	10	3	0	2010	10	3	12	
2	2010	10	12	18	2010	10	13	12	
3	2010	10	14	3	2010	10	14	15	
4	2010	10	20	15	2010	10	21	6	
5	2010	10	28	3	2010	10	28	21	
6	2010	11	2	18	2010	11	4	12	
7	2010	11	13	6	2010	11	15	6	
8	2010	11	16	6	2010	11	16	21	
9	2010	11	18	3	2010	11	19	0	
10	2010	11	25	21	2010	11	27	0	
11	2010	11	30	3	2010	11	30	21	
12	2010	12	4	21	2010	12	5	15	
13	2010	12	11	21	2010	12	12	12	
14	2010	12	16	15	2010	12	18	3	
15	2010	12	22	6	2010	12	23	9	
16	2010	12	25	6	2010	12	25	21	

the remote wind effect, and salt transported through Industrial Canal and Chef Menteur is controlled by the local wind.

Circulation patterns and velocity magnitude in the shallow western interior of Lake Pontchartrain and the coastal regions are dominated by

local winds. However, remote wind effect is responsible for the inflow or outflow through the inlets and controls the magnitude of the current velocity in the eastern region close to the open boundary (explaining almost 100% of the total variation). As a result, the further away from

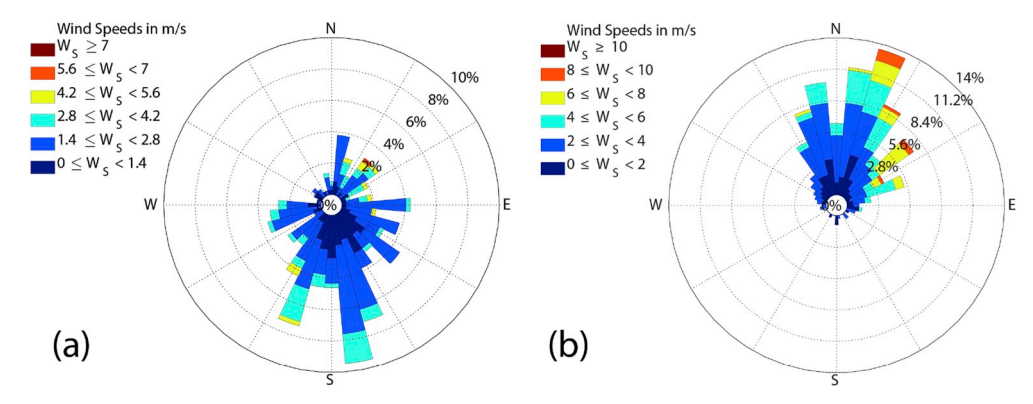


Fig. 14. Probability of occurrence (%) per degree of wind direction and velocity magnitude based on hourly wind data obtained from NDBC station (NWCL1 NO. 8761927) for the time period before- (a) and after- (b) the 16 cold front passages.

 $\begin{tabular}{ll} \textbf{Table 5}\\ R^2 \ and \ standard \ deviation \ for \ the \ approximation \ of \ surface \ slope \ in \ cross-estuary \ (N-S) \ and \ along-estuary \ (W-E) \ directions \ under \ corresponding \ wind \ directions \ using \ quasi-steady \ state \ equation \ before \ and \ after \ each \ cold \ front \ passage. \end{tabular}$ 

	Before		After		
	Cross- estuary	Along- estuary	Cross- estuary	Along- estuary	
	$R^2$	$\mathbb{R}^2$	$\mathbb{R}^2$	$\mathbb{R}^2$	
1	0.87	0.64	0.95	0.00	
2	0.00	0.94	0.00	0.67	
3	0.00	0.99	0.97	0.99	
4	0.74	0.00	0.71	0.57	
5	0.99	0.81	0.97	0.87	
6	0.00	0.00	0.99	0.50	
7	0.97	0.94	0.73	0.77	
8	0.00	0.93	0.00	0.83	
9	0.87	0.96	0.31	0.96	
10	0.99	0.71	0.98	0.00	
11	0.51	0.86	0.50	0.88	
12	0.10	0.43	0.54	0.08	
13	0.00	0.99	0.28	0.90	
14	0.99	0.97	0.99	0.91	
15	0.99	0.53	0.98	0.00	
16	0.81	0.00	0.64	0.18	
Average R <sup>2</sup>	0.55	0.67	0.66	0.57	
Standard deviation	0.46	0.37	0.35	0.39	

the open boundary, the less impact from the remote wind effect. The reason for the difference in remote wind effect in different regions is that the open boundaries are all on the eastern side, making the remote wind effect generally the strongest there, which subsequently dissipates away from the open boundary. Salinity distribution is mostly determined by remote wind effect. This is because salt is transported into the lake by the water exchanges through three inlets which are mainly controlled by the remote wind.

When compared with model results, the surface slopes approximated by the quasi-steady state equation lead to high R<sup>2</sup> values

(0.95–0.97) under local wind when tidal effects are not included at the open boundary. The high  $\rm R^2$  values indicate that the subtidal surface slopes are mainly controlled by local winds, consistent with the non-stratified model results. When tide is included from the open boundary, however, the  $\rm R^2$  value in the along-estuary direction is drastically reduced to  $\sim\!0.60$ . The reason of the reduction is that the tidally induced surface slope (Li and O'Donnell, 1997) adds an extra constant to the quasi-steady state balance in the along-estuary direction. When tidal effect is removed, the open boundary still reduces the accuracy of the quasi-steady state balance to some extent. Consequently, the further away from the open boundary, the smaller the influence and the larger the  $\rm R^2$  values.

The results also demonstrate that the frequency of dominant wind direction affects the  $R^2$  values of the quasi-steady state balance. When the cross-estuary (north-south directed) wind is dominant, the quasi-steady state balance is more accurate in that direction; same for the along-estuary direction. In addition, the  $R^2$  values are higher in the cross-estuary (north-south) direction than that in the along-estuary (east-west) direction after the cold front passages when the wind is the strongest and mostly from the northern quadrants.

#### Acknowledgement

We appreciate the help from the FVCOM team especially Dr. Changsheng Chen at the University of Massachusetts, Dartmouth for their generous assistance on the use of FVCOM. We appreciate the support of the Louisiana Optical Network Infrastructure (LONI) Management Council and LONI Network Operation Center staff at LSU for allowing us the access and use of the LONI super computers for the numerical simulation for this and related work. The study was also partly supported by National Science Foundation (OCE-1736713, OCE-0554674, DEB-0833225, OCE-1140307, EAR-1139997). Data support was provided by the Wave-Current-Surge Information System (WAVCIS), part of the Gulf Coastal Ocean Observing System (GCOOS). Comments and suggestions from four anonymous reviewers helped a significant improvement of the presentation of this work.

#### Appendix A. Damping of remote wind effect due to bottom friction

Five extra experiments are conducted to confirm the damping of remote wind effect due to bottom friction using changing bottom coefficients (0.00001, 0.0005, 0.005). Figure A1 shows that the remote wind effect is able to reach the interior of the lake with drag coefficient smaller than normal, e.g. 0.00001 (Figs. A1a and A1b). The bottom friction is the main reason for the reduction of the remote wind effect in the interior of Lake Pontchartrain. The remote wind is almost damped and has very limited effect on the interior when the bottom friction coefficient is large (Figs. A1e and A1f).

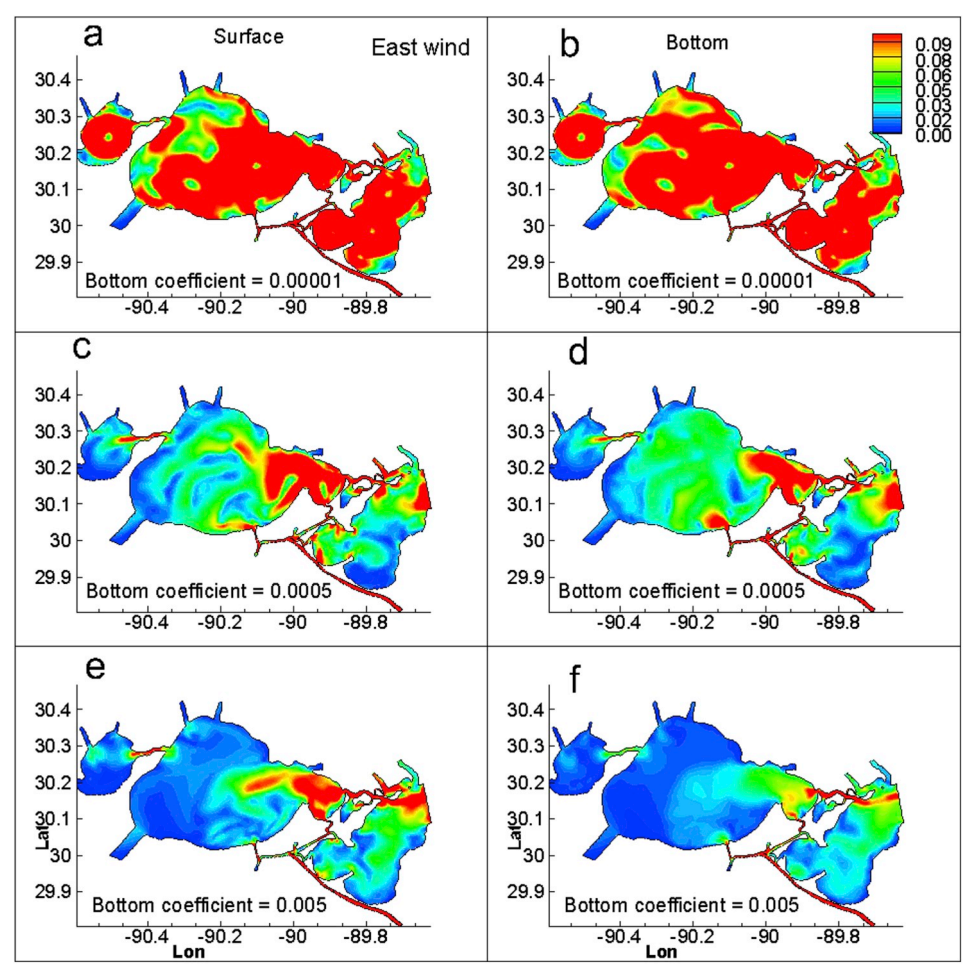


Fig. A1. Magnitude of surface and bottom velocity under different drag coefficient values ( $C_D = 0.00001$  for a and b, 0.0005 for c and d, 0.005 for e and f) under easterly wind. The left panels are for surface currents. The right panels are for bottom currents.

#### References

Allen, J.I., Somerfield, P.J., Gilbert, F.J., 2007. Quantifying uncertainty in high-resolution coupled hydrodynamic-ecosystem models. J. Mar. Syst. 64, 3–14.

Bianchi, T.S., Argyrou, M.E., 1997. Temporal and spatial dynamics of particulate organic carbon in the Lake Pontchartrain Estuary, Southeast Louisiana, U.S.A. Estuar. Coast Shelf Sci. 45, 557–569.

Bloesch, J., 1995. Mechanisms, measurement and importance of sediment resuspension in lakes. Mar. Freshw. Res. 46, 295–304.

Buijsman, M.C., Ridderinkhof, H., 2007. Water transport at subtidal frequencies in the Marsdiep inlet. J. Sea Res. 58, 255–268.

Casares-Salazar, R., Mariño-Tapia, I., 2016. Influence of the Remote Forcing and Local Winds on the Barotropic Hydrodynamics of an Elongated Coastal Lagoon. J. Coast. Res. 32 (1), 116–130.

Chen, C., Liu, H., Beardsley, R.C., 2003. An unstructured grid, finite-volume, three dimensional, primitive equation ocean model: application to coastal ocean and estuaries. J. Atmos. Ocean. Technol. 20, 159–186.

Chao, X., Jia, Y., Wang, S.S.Y., Hossain, A.K.M.A., 2012. Numerical modeling of surface flow and transport phenomena with applications to Lake Pontchartrain. Lake Reservoir Manag. 28 (1), 31–45. https://doi.org/10.1080/07438141.2011.639481.

Chuang, W.S., Swenson, E.M., 1981. Subtidal water variations in Lake Pontchartrain, Louisiana. J. Geophys. Res. 86 (C5), 4198–4204.

Cobb, M., Keen, T.R., Walker, N.D., 2008. Modeling the circulation of the Atchafalaya Bay system, part 2: River plume dynamics during cold fronts. J. Coast. Res. 24 (4), 1048–1062 West Palm Beach (Florida), ISSN 0749-0208. Crout, R.L., Hamiter, R.D., 1981. Response of bottom waters on the west Louisiana shelf to transient wind events and resulting sediment transport. Gulf Coast Assoc. Geol. Soc. 31, 273–278.

Csanady, G.T., 1968a. Wind-driven summer circulation in the Great Lakes. J. Geogr. Res. 73 (8), 2579–2589.

Csanady, G.T., 1968b. Motions in a model Great Lake due to a suddenly imposed wind. J. Geogr. Res. 73 (20) 7435-6447.

Csanady, G.T., 1973. Wind induced barotropic motions in long lakes. J. Phys. Oceanogr. 3, 429–438.

de Boer, J.P., Maas, L.R., 2011. Amplified exchange rate by tidal forcing of a piecewise-linear Helmholtz bay. Ocean Dynam. 61 (12), 2061–2072.

Dzwonkowski, B., Wong, K.-C., Ullman, W.J., 2014. Water level and velocity characteristics of a salt marsh channel in the Murderkill estuary, Delaware. J. Coast. Res. 30 (1), 63–74 Coconut Creek (Florida), ISSN 0749-0208.

Elliott, A.J., 1978. Observations of the Meteorologically Induced Circulation in the Potomac Estuary. Estuarine and Coastal Marine Science, vol. 6. pp. 285–299.

Engelund, F., 1973. Steady Wind Set-Up in Prismatic Lakes, Reprinted in Environmental Hydraulics: Stratified Flows (Lecture Notes on Coastal and Estuarine Studies. In: In: Pedersen, F.B. (Ed.), vol. 18. Springer, pp. 205–212 1986 (1973).

Falconer, R.A., George, D.G., Hall, P., 1991. Three-dimensional numerical modelling of wind-driven circulation in a shallow homogeneous lake. J. Hydrol. 124, 59–79.

Feng, Z., Li, C., 2010. Cold-front-induced Flushing of the Louisiana Bays. J. Mar. Syst. 82, 252–264

Filadelfo, R., Wilson, R.E., Gomez-Reyes, E., 1991. Subtidal eulerain currents in the upper and lower East River tidal strait: spring 1981. J. Geophys. Res. 96 (C8),

- 15217-15226.
- Galperin, B., Kantha, L.H., Hassid, S., Rosati, A., 1988. A quasi-equilibrium turbulent energy model for geophysical flows. J. Atmos. Sci. 45, 55–62.
- Garvine, R.W., 1985. A simple model of estuarine subtidal fluctuations forced by local and remote wind stress. J. Geophys. Res. 90 (C6), 11945–11948. https://doi.org/10. 1029/JC090iC06p11945.
- Garvine, R.W., 1991. Subtidal frequency estuary-shelf interaction: observations new Delaware Bay. J. Geophys. Res. 96 (C4), 7049–7064.
- Georgiou, I.Y., 2002. Three-Dimensional Hydrodynamic Modeling of Salinity Intrusion and Circulation in Lake Pontchartrain. University of New Orleans, Doctoral thesis, New Orleans, Louisiana, pp. 171p.
- Georgiou, I.Y., Retana, A.G., McCorquodale, J.A., Schindler, J., Fitzgerald, D.M., Hughes, Z., Howes, N., 2009. Impact of multiple freshwater diversions on the salinity distribution in the Pontchartrain Estuary under tidal forcing. J. Coast. Res. SI (54), 59–70 West Palm Beach (Florida), ISSN 0749-0208.
- Gibbs, M., Abell, J., Hamilton, D., 2016. Wind forced circulation and sediment disturbance in a temperate lake. N. Z. J. Mar. Freshw. Res. 50 (2), 209–227. https://doi.org/10.1080/00288330.2015.1116998.
- Guo, X., Valle-Levinson, A., 2008. Wind effects on the lateral structure of density-driven circulation in Chespeake Bay. Cont. Shelf Res. 28, 2450–2471.
- Haralampides, K., 2000. A Study of the Hydrodynamics and Salinity Regimes of the Lake Pontchartrain System. Ph.D. dissertation, Univ. of New Orleans, pp. pp219.
- Herrling, G., Winter, C., 2015. Tidally- and wind-driven residual circulation at the multiple-inlet system East Frisian Wadden Sea. Cont. Shelf Res. 106, 45–59.
- Huang, H., Chen, C., Cowles, G.W., Winant, C.D., Beardsley, R.C., Hedstrom, K.S., Haidvogel, D.B., 2008. FVCOM validation experiments: Comparisons with ROMS for three idealized barotropic test problems. J. Geophys. Res. 113, C07042. https://doi. org/10.1029/2007JC004557.
- Huang, H., Justic, D., Lane, R.R., Day, J.W., Cable, J.E., 2011. Hydrohynamic response of the Breton Sound estuary to pulsed Mississippi River inputs, Estuarine. Estuar. Coast Shelf Sci. 95, 216–231.
- Huang, W., Li, C., 2017. Cold Front Driven Flows through Multiple Inlets of Lake Pontchartrain Estuary. J. Geophys. Res.
- Keddy, P.A., Campbell, D., McFalls, T., Shaffer, G., Moreau, R., Dranguet, C., Heleniak, R., 2007. The wetlands of lakes Pontchartrain and Maurepas: past, present and future. Environ. Rev. 15, 1–35 Table 2.
- Kemp, G.P., J. T, Wells, van Heerden, I.L., 1980. Frontal passages affect delta development in Louisiana. Coastal Oceanography and Cimatological News 3, 4–5.
- Li, C., Chen, C., 2014. Shelf circulation prior to and post a cold front event measured from vessel-based acoustic Doppler current profiler. J. Mar. Syst. 139, 38–50.
- Li, C., Huang, W., Chen, C., Lin, H., 2018a. Flow regimes and adjustment to wind-driven motions in Lake Pontchartrain: a modeling experiment using FVCOM. J. Geo. Res. Oceans 123, 8460–8488. https://doi.org/10.1029/2018JC013985.
- Li, C., O'Donnell, J., 1997. Tidally induced residual circulation in estuaries with lateral depth variation. J. Geophys. Res. 102 (27) 915 - 927,929.
- Li, C., Walker, N., Hou, A., Georgiou, I., Roberts, H., Laws, E., McCorquodale, J., Weeks, E., Li, X., Crochet, J., 2008. Circular plumes in Lake Pontchartrain estuary under wind straining, *Estuarine*. Estuar. Coast Shelf Sci. 80, 161–172.
- Li, C., Weeks, E., Blanchard, B.W., 2010. Storm surge induced flux through multiple tidal passes of Lake Pontchartrain estuary during Hurricanes Gustav and Ike, *Estuarine*. Estuar. Coast Shelf Sci. 87, 517–525.
- Li, C., Weeks, E., Huang, W., Milan, B., Wu, R., 2018b. Weather Induced Transport through a Tidal Channel Calibrated by an Unmanned Boat. J. Atmos. Ocean. Technol. 35 (2), 261–279.
- Li, C., Boswell, K.M., Chaichitehrani, N., Huang, W., Wu, R., 2019a. Weather induced subtidal flows through multiple inlets of an Arctic micro-tidal lagoon. Acta Oceanol. Sin. 38 (3), 1–16. https://doi.org/10.1007/s13131-019-1361-2.
- Li, C., Huang, W., Milan, B., 2019b. Atmospheric cold front induced exchange flows through a microtidal multi-inlet bay: analysis using multiple horizontal ADCPs and FVCOM simulations. J. Atmos. Ocean. Technol. 36, 443–472. https://doi.org/10. 1175/JTFCH-D-18-0143 1
- Li, C., Zheng, Q., 2016. Breakdown of Hydrostatic Assumption in Tidal Channel with Scour Holes. Frontiers (Marine Science) 3, 199. https://doi.org/10.3389/fmars.2016. 00100
- Lin, J., Li, C., Boswell, K.M., Kimball, M., Rozas, L., 2016. Examination of Winter Circulation in a Northern Gulf of Mexico Estuary. Estuar. Coasts 39, 1–21. https://doi.org/10.1007/s12237-015-0048-y.
- Liu, C., Cowles, G.W., Churchill, J.H., Stokesbury, K.D.E., 2015. Connectivity of the bay scallop (Argopecten irradians) in Buzzards Bay, Massachusetts, U.S.A. Fish. Oceanogr. 24 (4), 364–382.
- McCorquodale, J.A., Rachel, J.R., Georgiou, I.Y., Haralampides, K.A., 2009. Salinity, nutrient, and sediment dynamics in the Pontchartrain Estuary. J. Coast. Res. (0749-0208) SI (54), 71–78 West Palm Beach (Florida).
- Mellor, G.L., Yamada, T., 1982. Development of a turbulence closure model for

- geophysical fluid problem. Rev. Geophys. Space Phys. 20, 851-875.
- Moeller, C.C., Huh, O.K., Roberts, H.H., Gumley, L.E., Menzel, W.P., 1993. Response of Louisiana coastal environments to a coastal front passage. J. Coast. Res. 9 (2), 434–447.
- O'Connell, M.T., O'Connell, A.M.U., Schieble, C.S., 2014. Response of Lake Pontchartrain Fish Assemblages to Hurricanes Katrina and Rita. Estuar. Coasts 37, 461–475. https://doi.org/10.1007/s12237-013-9675-3.
- Penland, S., Beall, A., Kindinger, J., 2002. Environmental Atlas of the Lake Pontchartrain Basin: Lake Pontchartrain Basin Foundation, New Orleans, LA, US Geol. Survey Open File Report 02-xxx. CD-ROM (available at: http://coastal.er.usgs.gov/pontchartrain/
- Proudman, J., 1953. Dynamical Oceanography. Wiley, London, pp. 409.
- Ralston, D.K., Geyer, W.R., Lerczak, J.A., 2008. Subtidal Salinity and Velocity in the Hudson River Estuary: Observations and Modeling. J. Phys. Oceanogr. 38, 753–770. https://doi.org/10.1175/2007JPO3808.1.
- Roberts, H.H., Huh, O.K., Hsu, S.A., Rouse Jr., L.J., Rickman, D., 1989. Winter storm impacts on the Chenier Plain Coast of Southwestern Louisiana. Gulf Coast Assoc. Geol. Soc. 39, 515–522.
- Roberts, H.H., DeLaune, R.D., White, J.R., Li, C., Sasser, C.E., Braud, D., Weeks, E., Khalil, S., 2015. Floods and cold front passages: Impacts on coastal marshes in a river diversion setting (Wax Lake delta area, Louisiana). J. Coast. Res. (0749-0208) 31 (5), 1057–1068 Coconut Creek (Florida).
- Roy, E.D., Ngyuyen, N.T., Bargu, S., White, J.R., 2012. Internal loading of phosphorus from sediments of Lake Pontchartrain (Louisiana, USA) with implications for eutrophication. Hydrobiologia 684, 69–92. https://doi.org/10.1007/s10750-011-00000
- Sanay, R., Valle-Levinson, A., 2005. Wind-induced circulation in semienclosed homogeneous, rotating basins. J. Phys. Oceanogr. 35, 2520–2531.
- Scheffer, M., 2004. The Ecology of Shallow Lakes. Kluwer Academic., pp. 357.
- Schoen, J.H., Stretch, D.D., Tirok, K., 2014. Wind-driven circulation patterns in a shallow estuarine lake: St Lucia, South Africa. Estuarine. Estuar. Coast Shelf Sci. 146, 49–59.
- Scully, M.E., Friedrichs, C., Brubaker, J., 2005. Control of estuarine stratification and mixing by wind-induced straining of the estuarine density field. Estuaries 28 (3), 321–326.
- Signell, R.P., List, J.H., 1997. Modeling Waves and Circulation in Lake Pontchartrain, Louisiana. Gulf Coast Association of Geological Soceities Transactions 47, 529–532.
- Smith, N.P., 1977. Meteorological and tidal exchanges between Corpus Christi Bay, Texas, and Northwestern Gulf of Mexico. Estuar. Coast Mar. Sci. 5, 511–520.
- Snedden, G.A., Cable, J.E., Wiseman Jr., W.J., 2007. Subtidal sea level variability in a shallow Mississippi River deltaic estuary, Louisiana. Estuar. Coasts 30 (5), 802–812.
- Swenson, E.M., Chuang, W.S., 1983. Tidal and subtidal water volume exchange in an estuarine system. Estuar. Coast Shelf Sci. 16, 229–240.
- Walker, N.D., Hammack, A.B., 2000. Impacts of winter storms on circulation and sediment transport: Achafalaya-Vermilion Bay region, Louisiana, U.S.A. J. Coast. Res. (0749-0208) 16 (4), 996–1010 West Palm Beach (Florida).
- Wang, D.-P., Elliott, A.J., 1978. Non-tidal variability in the Chesapeake Bay and Potomac River: evidence for non-local forcing. J. Phys. Oceanogr. 8, 225–232.
- Weeks, E., Robinson, M.E., Li, C., 2018. Quantifying cold front induced water transport of a bay with *in situ* observations using manned and unmanned boats. Acta Oceanol. Sin. 37 (11), 1–7. https://doi.org/10.1007/s13131-018-1330-1.
- White, J.R., Fulweiler, R.W., Li, C., Bargu, S., Walker, N.D., Twilley, R.R., Green, S.E., 2009. Mississippi River flood of 2008: observations of a large freshwater diversion on physical, chemical, and biological characteristics of shallow estuarine lake. Environ. Sci. Technol. 43 (15), 5599–5604.
- Wong, K.C., 1994. On the nature of transverse variability in a coastal plain estuary. J. Geophys. Res. 99 (C7), 14209–14222.
- Wong, K., 2002. On the wind-induced exchange between Indian River Bay, Delaware and the adjacent continental shelf. Cont. Shelf Res. 22, 1651–1668.
- Wong, K.C., 1987. Subtidal volume exchange through the Chesapeake and Delaware Canal. J. Geophys. Res. 92 (C10), 10870–10874.
- Wong, K.C., Valle-Levinson, A., 2002. On the relative importance of the remote and local wind effects on the subtidal exchange at the entrance to the Chesapeake Bay. J. Mar. Res. 60, 477–498.
- Wong, K.C., Dzwonkowski, B., Ullman, W.J., 2009. Temporal and spatial variability of sea level and volume flux in the Murderkill Estuary. Estuar. Coast Shelf Sci. 84, 440–446.Wong, K.C., Garvine, R.W., 1984. Observations of wind-induced, subtidal variability in the Delaware Estuary. J. Geophys. Res. 89 (C6), 10589–10597.
- Wong, K.C., Moses-Hall, J.E., 1998. On the relative importance of the remote and local wind effects to the subtidal variability in a coastal plain estuary. J. Geophys. Res. 103 (C9), 18393–18404.
- Wu, H., Zhu, J.R., Shen, J., Wang, H., 2011. Tidal modulation on the Changjiang River plume in summer. J. Geophys. Res. 116 (C08017), 2011. https://doi.org/10.1029/ 2011JC007209.